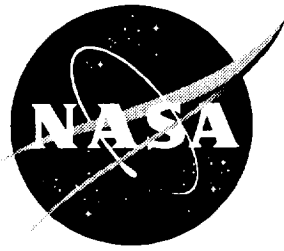


Structural Analysis and Testing of an Erectable Truss for Precision Segmented Reflector Application

Timothy J. Collins, W. B. Fichter, Richard R. Adams, and Mehzaad Javeed



Structural Analysis and Testing of an Erectable Truss for Precision Segmented Reflector Application

Timothy J. Collins, W. B. Fichter, and Richard R. Adams
Langley Research Center • Hampton, Virginia

Mehzad Javeed
Lockheed Engineering & Sciences Company • Hampton, Virginia

The use of trademarks or names of manufacturers in this report is for accurate reporting and does not constitute an official endorsement, either expressed or implied, of such products or manufacturers by the National Aeronautics and Space Administration.

Available electronically at the following URL address: <http://techreports.larc.nasa.gov/ltrs/ltrs.html>

Printed copies available from the following:

NASA Center for AeroSpace Information
800 Elkridge Landing Road
Linthicum Heights, MD 21090-2934
(301) 621-0390

National Technical Information Service (NTIS)
5285 Port Royal Road
Springfield, VA 22161-2171
(703) 487-4650

Abstract

This paper describes analysis and test results obtained at Langley Research Center (LaRC) on a doubly curved test-bed support truss for precision reflector applications. Descriptions of test procedures and experimental results that expand upon previous investigations are presented. A brief description of the truss is given, and finite-element-analysis models are described. Static-load and vibration test procedures are discussed, and experimental results are shown to be repeatable and in generally good agreement with linear finite-element predictions. Truss structural performance (as determined by static deflection and vibration testing) is shown to be predictable and very close to linear. Vibration test results presented herein confirm that an anomalous mode observed during initial testing was due to the flexibility of the truss support system. Photogrammetric surveys with two 131-in. reference scales show that the root-mean-square (rms) truss-surface accuracy is about 0.0025 in. Photogrammetric measurements also indicate that the truss coefficient of thermal expansion (CTE) is in good agreement with that predicted by analysis. A detailed description of the photogrammetric procedures is included as an appendix.

Introduction

An objective of the NASA Precision Segmented Reflector (PSR) program has been to develop techniques for design, testing, fabrication, and assembly of orbiting instruments that will be used for both astrophysical and Earth observations. Applications for such instruments include submillimeter astronomical observatories (fig. 1), microwave radiometers, and communications antennas. These instruments generally require extremely accurate surfaces for operation at near-optical wavelengths.

A common requirement for space-based observatories (reflectors) is an accurate, stiff, lightweight support structure; therefore, in the PSR program, considerable effort has been devoted to the design, fabrication, and testing of a 13-ft-diameter (4-m-diameter) test-bed truss. The truss, designed for on-orbit astronaut assembly, has a doubly curved geometry to accommodate an assemblage of parabolic reflector panels. A major goal of the PSR program was the fabrication of a truss that would exhibit linear, predictable structural behavior, and highly accurate surface node placement without postassembly adjustment.

Details of the design and fabrication of the erectable truss are presented in reference 1, along with an evaluation of static and dynamic performance and comparisons with analytical predictions. This paper contains the results of additional testing and analysis of the truss, which was conducted for the following purposes: (1) to obtain a more detailed characterization of truss static performance (including truss deflection and member strains under static loading), (2) to investigate anomalous vibration results that were previously reported in reference 1,

(3) to obtain more accurate photogrammetric surface-accuracy measurements, and (4) to measure the truss coefficient of thermal expansion. Although this paper is largely self-contained, it can be considered a continuation of reference 1. Hence, the results presented are, for purposes of comparison, sometimes related to those presented previously. Some additional details related to the analysis models and test methods are included in this paper. Table 1 lists the tests that are discussed in the present paper and indicates those tests that were first presented in reference 1.

This report begins with a brief description of the truss, including its geometry and component parts, after which finite-element models that are used to analyze the truss are described. Static-load and vibration test results are presented and compared with analytical predictions. Also presented are the results of photogrammetric (surface-accuracy) surveys conducted at three ambient temperatures. The first of these surveys, in which a single 75-in-long reference scale was used, was reported in reference 1. In the remaining two surveys, reported for the first time in this paper, two 131-in-long scales were used. The photogrammetric survey results are also used to determine an average coefficient of thermal expansion (CTE) of the truss. The effect of modeling uncertainties on the interpretation of the photogrammetric results is also considered.

Symbols and Abbreviations

DCDT	direct-current displacement transducer
E	modulus of elasticity, psi
EA	extensional stiffness, lb
MAC	modal assurance criterion

PSR	precision segmented reflector
rms	root mean square
T	temperature, °F
X, Y, Z	rectangular Cartesian truss coordinates
x, y	photogrammetric image coordinates

Truss Description

The truss structure is shown in figures 2(a) and 2(b). The truss has a tetrahedral geometry and consists of 150 graphite-epoxy tubular struts connected at 45 aluminum nodes. The total mass of the truss structure is 189 lbm. The tubular struts have an outer diameter of 1.0 in. (different line widths are used in fig. 2(b) for clarity) and are composed of 12 plies of T300/5208 graphite-epoxy material in a $\pm 10^\circ$ lay-up. The distance between node centers ranges from 30.37 in. to 31.73 in. for concave-surface struts and from 34.53 in. to 36.09 in. for convex-surface struts. All core struts have a length (measured between node centers) of 32.03 in. In planform view, the truss has a maximum diameter of 153.9 in.

The concave-surface nodal locations are prescribed to accommodate a center-fed parabolic reflector with a focal length of 94.5 in. (2.4 m). The truss is fabricated such that all concave-surface node centers are 5.91 in. (15 cm) along a surface normal behind the required parabolic surface. Thus, unlike the required reflector surface, the node centers are not intended to lie in a parabolic surface. As was done in reference 2, it is possible to determine a paraboloid that best fits, in a least-squares sense, the coordinates of the node centers. However, the shape of such a paraboloid will only approximate that of the truss surface, and its focal length should not be expected to match that of the true reflector surface. An additional characteristic of the erectable truss is its "threefold" symmetry about the Z-axis (fig. 2(b)). As a consequence of this symmetry, any 120° segment of the truss (measured in the X-Y plane) can be successively replicated and rotated twice to generate the entire truss geometry.

Figure 3 shows the configuration of the tube, joints, and nodes in a typical test-bed strut assembly. Each node is a partial sphere with one large flat surface and nine strut attachment locations. The large flat surface is used as a reference plane during node fabrication; after truss assembly, it facilitates the mounting of reflective panels or peripheral hardware. The joint assemblies were designed for stiffness, linear load-displacement behavior, and compatibility with on-orbit astronaut assembly. Table 2 is a summary of the important structural characteristics of the components shown in figure 3. Details concerning the truss geometry, the design of the nodes and joints, and the method used to set the strut assem-

blies to prescribed lengths are contained in reference 1 and are not repeated here.

Several tests have been performed at Langley Research Center (LaRC) to determine the stiffness properties of the individual components that make up each strut assembly (ref. 1). These tests determine the axial and bending stiffnesses of a typical joint-node combination and of the tubular struts. The joint-node axial stiffness was determined by testing two joints and one node that are acting in series. (See ref. 1.) Figure 4 shows load-displacement test results for a typical joint-node specimen and for a tubular strut. In both cases, the load-displacement behavior is essentially linear. The extensional stiffness (Modulus \times Area) of the joint-node assemblies is 1.9×10^6 lb, and the extensional modulus of the individual struts is 16.9×10^6 psi. These extensional properties, along with the other component properties listed in table 2, were used to formulate finite-element models for truss analysis.

Truss Analysis Models

Reference 1 describes three finite-element models that were used to analyze the truss. The simplest of these models used one extensional element (axial stiffness only) to connect two grid points that were located at the truss node centers. To account for the aluminum joints and nodes in the truss, each strut-joint-node combination was modeled as a single element with an effective axial stiffness and effective coefficient of thermal expansion equal to those of the individual components acting in series. This procedure is described in reference 3. The masses of the joints and nodes were incorporated by placing lumped-mass elements at the node center locations. Other nonstructural mass that was required for testing was included in a similar manner.

In addition to the simplified model just described, two more-refined models were used for evaluation of the truss structure. These models, discussed in reference 1, included both extensional and bending properties. Bending-stiffness properties for the joint-node combinations and struts are contained in reference 1. The refined models offer an advantage over the simplified model because they can more accurately predict higher frequency truss vibration modes (ref. 1) that involve bending of the individual struts. When other aspects of truss structural performance were analyzed, including static deflection, surface accuracy, thermal distortion, and lower frequency vibration models, the simplified finite-element model yielded essentially the same predictions as the refined models. Unless otherwise noted, analytical results presented herein were obtained with the simplified (no strut bending) model.

Static Tests

Test Description

Figure shows a planform diagram of the experimental setup used for truss static testing. The truss was supported at three nodes on the convex truss surface (solid circles). The truss was bolted to three mounting fixtures (fig. 5(b)), which were bolted to a large steel table (10 ft by 4 ft by 2 ft) that weighed approximately 13000 lb. It was intended that this support system achieve a good approximation to clamped boundary conditions at the three support nodes. The steel table was used to minimize motion of the support points during static and dynamic testing. The location and size of the table with respect to the truss are indicated in figure 5(a).

The support system used for the tests reported in reference 1 consisted of three trunnion mounts (fig. 5(b)). The trunnions were bolted to a lighter (9000 lb) table than that used for the present tests. The four clevis bolts remained loose until just before each test, so the trunnion pins could rotate (about an axis perpendicular to the truss radius) to reduce preloading of the structure that was caused by the mounting process or by changes in ambient temperature. The clevis bolts were tightened immediately before each test. However, the initial static and dynamic tests revealed that these trunnion mounts exhibited noticeable flexibility (even after the tightening of the clevis bolts) that could not be accurately modeled or predicted by analysis. Therefore, for the tests reported herein, the trunnion mounts were replaced by the mounting fixtures shown in figure 5(b).

The truss was statically loaded by applying vertical (deadweight) loads that ranged from 20 lbf to 100 lbf, in 20-lb increments, at the six "corner" nodes shown in figure 5(a). Specially designed weight hangers (fig. 6) were used to insure that the loads acted through the spherical center of each node.

In each of the three truss regions (R1, R2, and R3 in fig. 5(a)), six nodes were instrumented with direct-current displacement transducers (DCDT's), as shown in figure 7, and nine struts were instrumented with strain-gage triads. It was convenient to identify three truss regions; because of the threefold truss symmetry mentioned previously, R1, R2, and R3 represent nominally identical portions of the truss. The DCDT and strain-gage locations shown in figure 5(a) were chosen to adhere to the same symmetry. The DCDT's measured the vertical (Z direction in fig. 2(b)) displacement at the six nodes. The strain-gage triads, which consisted of three independent strain gages equally spaced around the strut circumference, were located at the midlength of the struts. The axial strain in a particular strut was computed as the average of the strains in the three strain gages that

made up each triad. In figure 5, the DCDT's are labeled D1 to D6, and the strain-gage triads are labeled S1 to S9. The DCDT's had a full-scale displacement range of 0.05 in. with a maximum nonlinearity of ± 0.00025 in. at full scale.

Because of limitations on available instrumentation and data acquisition, data were collected in only one of the three truss regions during each loading sequence. Therefore, obtaining data for the complete truss required a series of three loading sequences, defined herein as a single test. Three static-load tests were conducted, each of which consisted of instrumenting and collecting data sequentially in all three truss regions. Thus, in each test, 18 displacement measurements and 27 axial-strain measurements were taken. Tests 1 and 2 involved the complete truss. For test 3, the six struts indicated in figure 5 were removed so that the effect of reduced truss redundancy on static deflection and structural predictability could be examined.

Results and Correlation With Analysis

Figure 8 is a comparison of measured and predicted nodal vertical displacements at the maximum loading condition of 100 lbf at each truss corner node. Displacement results for tests 1 and 2 are shown for each DCDT location within each truss region. Also shown are the displacements predicted from finite-element analysis. Because of symmetry in geometry and loading, predicted displacements (and strains) for corresponding locations within regions R1, R2, and R3 are the same.

The results of the second test were nearly identical to those of the first test. Deviations from predicted deflections ranged in magnitude from 0 to 0.0009 in. In relative terms, the largest deviations, about 16 percent in test 1 and 19 percent in test 2, occurred at DCDT location D6 in truss region R2. Relatively large deviations (>11 percent for both tests) also occurred at node locations D5 and D6 in region R1. These results are similar to those presented in reference 1, where maximum deviations of approximately 14 percent were observed at locations D5 and D6 in region R1. The reason for the larger differences at these node locations is unknown. At all other DCDT locations, the predicted displacements differed from the measured displacements by 8 percent or less, a result that is also consistent with reference 1. In figure 9, typical load-displacement curves are shown for test-1 node locations D1 and D2. In each static test, load-displacement response at all nodes was approximately linear, and there was only slightly discernible hysteresis.

A comparison of measured and predicted maximum nodal displacements for the truss with six struts removed (test 3) is shown in figure 10. For comparison, the corresponding predicted displacements for tests 1 and 2 (no

struts removed) are also shown. In test 3, deviations from predicted deflections ranged in magnitude from 0.0001 in. to 0.0040 in. Again, the largest differences in predicted displacements, 25.7 percent and 31.4 percent, occurred in region R1 at locations D5 and D6, respectively. At all other node locations, the differences between predicted and measured displacements were less than 14 percent, and nearly all differences greater than 10 percent occurred in truss region R1.

Figure 11 is a comparison of measured and predicted strain magnitudes at maximum loading (tests 1 and 2). Deviations from predicted strain magnitudes ranged from 0.1×10^{-6} in./in. to 6.7×10^{-6} in./in., and the greatest difference was in test 2 at location S1 in region R1. Figure 12 shows the test-1 load-strain response for struts S1 and S2 in region R1. These curves are typical and, as indicated by the data shown for S1, the degree of non-linearity was sometimes greater than that observed in the displacement measurements (fig. 9). In all tests, the measured strain magnitudes were less than 50×10^{-6} ; in many struts, the strains were much smaller (e.g., see triads S8 and S9). Such small strains are comparable in magnitude to the resolution of the strain gages and thus have a relatively large uncertainty associated with them. Adding to this uncertainty was a difference in thermal-expansion characteristics of the strain gages and the graphite-epoxy struts such that a temperature change of 1°F during a test could cause an apparent strain drift of approximately 6×10^{-6} .

Figure 13 shows strain measurements and predictions for the truss with six struts removed (test 3). Differences between measured and predicted strains are greater than in tests 1 and 2. The results indicate that the reduction in redundancy due to the removal of six struts degraded the predictability of truss structural performance. This degradation may have been caused by the effects of node rotation and/or eccentric strut loading, which were not included in any of the analysis models. However, the large differences between measured and predicted strains did not occur consistently in each truss region (e.g., compare S2 in each region); therefore, the differences could not be predicted by using a uniform refinement of the analysis models. Time constraints on testing did not allow further examination of these issues.

There is evidence that the static-test displacement measurements were influenced by rotation of the 13000-lb table to which the truss was mounted. For example, figure 14 shows the differences between measured and predicted vertical displacements for each static test; the figure also indicates whether a particular measured displacement was less than or greater than predicted. Measured displacements that are less than predicted are generally located on one side of the support

table, while measurements greater than predicted are on the other. However, figure 15 shows that the differences between measured and predicted strain magnitudes for each static test are, for the most part, randomly distributed relative to the support table. This result is consistent with a table rotation, which would affect measurements of displacement but not strain.

Vibration Tests—Normal Modes

This section describes three tests that were performed to characterize the dynamic response of the erectable support truss. Test 1 (ref. 1) consisted of a complete vibration test, wherein all 45 truss nodes were instrumented and nodal accelerations were measured along three orthogonal axes at each node. Test 2 (a repeat of test 1) was conducted with less instrumentation but with a heavier table and improved truss support fixtures. The primary purpose of test 2 was to isolate an anomalous mode that appeared in test 1. Finally, test 3 was conducted to approximate a free-free truss boundary condition. The results of all three tests are presented and correlated with linear finite-element predictions. The predicted frequencies in this section were obtained by using a finite-element model (ref. 1), which included strut bending. All dynamic analysis results were obtained by using linear finite-element models with the truss properties listed in table 2. Gravity preloading of the structure was not included in any of the dynamic analyses.

Test 1 Description

In this test, the truss was mounted by attaching the three convex-surface nodes (figs. 5(a) and 16) to the trunnion mounts described in figure 5(b). The trunnion mounts were secured to a support table that was approximately 6 ft by 6 ft and weighed approximately 9000 lb. This support table was smaller and lighter than the 13000-lb rectangular table described in the section entitled "Static Tests." Mode-shape results predicted from finite-element analysis were used to locate two shakers on the structure at the nodes indicated in figure 16. The shakers were attached to the structure at oblique orientations (fig. 17) to excite all the global structural modes of interest. The excitation signals consisted of burst random signals with a frequency spectrum of 0 to 250 Hz. The translational acceleration response of the structure was measured at all 45 nodes of the upper and lower truss surfaces along three orthogonal axes of the structure. One of the triaxial accelerometers is shown in figure 18. To mount the accelerometers along the truss definition axes (fig. 2(b)), the flat face of each node was fitted with an aluminum wedge of the appropriate angle. The added mass of these wedges was accounted for in all dynamic analyses.

A data-acquisition system was used to acquire and process the frequency-response-function data in the frequency range of 0 to 250 Hz. The SDRC I-DEAS Test™ software package (ref. 4) was used to analyze the test data.

Test 1 Results and Correlation With Analysis

Predicted and measured frequency and mode-shape results are presented in tables 3(a) and 3(b). Also included are the modal assurance criterion (MAC) values (ref. 4), which show the correlation between the deflection patterns of two mode shapes (i.e., a MAC value of 1.0 indicates perfect correlation between predicted and measured mode shapes). Finally, table 3(a) presents measured damping levels that are close to 1 percent of critical damping for each mode shape.

A comparison of test-1 and analysis results indicates good correlation except for mode 3, which was not predicted by analysis. The MAC values of modes 6 and 7 are relatively low. Inspection of the experimental mode shapes from test 1 indicated that the difference between the analysis and test results may be caused by the flexibility of the trunnion support fixtures, which was not accounted for in the finite-element model. This possibility was investigated further in test 2.

Test 2 Description

To investigate the effects of the trunnion support fixtures (fig. 5(b)) on the dynamic behavior of the truss, test 2 was conducted with the fixed-support fixtures (fig. 5(b)) and the heavier support table that were used for the tests described in the section "Static Tests." In retesting, only 15 of the 45 nodes were instrumented, and only accelerations in the Z direction (vertical) were measured.

Test 2 Results and Correlation With Analysis

Mode 3 of the experimental data from test 1 (51.9 Hz) was not observed in test 2 (table 4) with the redesigned support fixtures and heavier table. Therefore, it is concluded that this mode was caused by support-system flexibility and that the modified support fixtures effect a more nearly fixed boundary condition. Table 5 is a comparison of the natural frequencies from test 1, test 2, and the analysis model. It can be seen that the dynamic response of the structure is predictable and repeatable. The frequency values of test 2 show good correlation with analysis, and the MAC values from test 2 are slightly better than those from test 1 for all modes except mode 9, even though they are based on significantly fewer acceleration measurements.

Test 3 Approximated Free-Free Vibration

To approximate a free-free boundary condition, the structure was suspended from a crane by long cables. This test was performed merely to supplement the fixed-support tests—not to serve as a well-defined free-free vibration study. Several frequency-response functions were measured in this configuration. Table 6 is a comparison of test and analysis results for the first four modes of the approximate free-free configuration. Again, agreement between the analytical and experimental frequencies is good, and the MAC values indicate good mode-shape correlation.

Surface-Accuracy Tests—Photogrammetry

This section of the paper is a summary of the results of photogrammetric surveys that were used to characterize the truss surface. See the appendix for a more detailed description of the procedures used to obtain these photogrammetric measurements.

Test Description

After the photogrammetric survey described in reference 1, two additional surveys of the upper truss surface were performed. The additional surveys were conducted with longer and more accurate reference scales to verify results obtained in the first survey, in which a single, shorter scale was used. Also, the additional surveys were performed at different temperatures to determine the thermal-expansion characteristics of the truss. The procedure for these surveys was similar to that described in reference 1. Reflective targets with a diameter of 0.1 in. were centered on the flat surface of each upper-surface node. A stationary elevated photogrammetric camera was used to photograph the truss, which was rotated about its vertical axis in 15° increments to provide 24 distinct perspectives. Figure 19 shows the camera positioned above the truss, which rests on the large steel table on which it was rotated.

Finite-element analyses that included both gravitational and thermal truss distortions were performed to obtain target-coordinate predictions. Thermal distortions were caused by a temperature change between assembly and testing of the truss. The truss was assembled at a temperature of 69°F, while the photogrammetric surveys reported in reference 1 and in this paper were performed at temperatures of 72.6°F (survey 1, ref. 1), 77.5°F (survey 2), and 63.0°F (survey 3). In reference 1, a tolerance on individual strut lengths of ± 0.0002 in. was assumed. Subsequently, a small number of length-setter repeatability tests indicated that strut-length tolerance was probably an order of magnitude greater (about ± 0.002 in.). Recent adjustments to the length-setter hardware have reduced this tolerance considerably.

In surveys 2 and 3, a reference scale for each photograph was established by placing two low-CTE graphite-epoxy tubes (about 131 in. long) in the field of view of the photogrammetric camera. In survey 1, which was first reported in reference 1, only one relatively short (about 75 in. long) reference scale was used. Prior to the photogrammetric surveys, each 131-in. tube was configured with colinear reflective targets similar to those centered on the upper-surface truss nodes. The distances between reference-scale targets were measured independently with a laser interferometer. These measurements provided the reference scale for the photogrammetric surveys. Measurements from the photographs, along with target-coordinate predictions from finite-element analyses, were used to assess the root-mean-square (rms) difference between the predicted and photographed target locations.

Initial interferometry-based measurements of the reference scales made at LaRC differed by about 0.01 in. from similar measurements made later with a coordinate-measuring machine at the Jet Propulsion Laboratory (JPL). Investigation revealed that initial LaRC measurements were in error because of a nonoptimum laser interferometer measurement procedure. After modification of the procedure, additional reference-scale measurements were made at LaRC and agreed well (within 0.0007 in.) with the JPL measurements. These later measurements were used to obtain the photogrammetric results presented herein for surveys 2 and 3.

Results and Correlation With Analysis

Figure 20 shows the rms differences between the predicted and photogrammetrically measured target coordinates. In the figure, an rms difference is shown for each truss coordinate along with a "grand" rms difference that was obtained by considering all 81 coordinate differences (3 coordinates for each of 27 upper-surface truss nodes) as statistical variables. The grand rms difference is defined by the photogrammetric system described in the appendix and is obtained by using a six-parameter transformation (six rigid-body motions). Because the grand rms difference is obtained by treating all 81 coordinates as independent variables, it is possible for the grand rms difference to be less than the rms difference for the individual X, Y, and Z coordinates.

The grand rms differences of surveys 2 and 3 are slightly smaller than those reported in reference 1 for survey 1. This improvement is most likely caused by the use of two longer and more precisely measured reference scales. For surveys 2 and 3, the grand rms difference is approximately 0.0025 in. The greatest contributors to the differences between predicted and measured target coordinates are probably errors in setting the lengths of the

strut assemblies. In fact, the observed grand rms differences (about 0.0025 in.) are consistent with the increased strut tolerance (about ± 0.002 in.) mentioned previously in this section. Other possible causes of the observed differences are uncertainties in the photogrammetric procedure itself and in the finite-element models used to determine the predicted truss shapes. However, the theoretical tolerance of the photogrammetric measurements was between ± 0.0003 in. and ± 0.0006 in., and the impact of uncertainties in the finite-element-analysis models (discussed in detail at the end of this section) was relatively small. All three surveys show the grand rms difference to be less than the PSR design goal of 0.004 in.

The results of the three photogrammetric surveys were used to obtain an overall coefficient of thermal expansion for the truss by comparing as-measured with as-predicted truss diameters as a function of survey temperature. (See fig 21.) The figure shows truss diameters (d_1 , d_2 , and d_3), determined from the photogrammetric surveys, as a function of temperature. The slope of each line represents the measured rate of truss expansion with temperature and, when divided by the truss diameter, roughly equates to the measured truss CTE. The predicted truss diameter as a function of temperature is also shown. The measured rate of truss expansion with temperature (truss CTE), as determined from the average of the three experimental curves in figure 21, is about $4.2 \times 10^{-6}/^{\circ}\text{F}$. This value differs from that predicted by analysis ($4.6 \times 10^{-6}/^{\circ}\text{F}$) by 8.5 percent. The CTE of the graphite-epoxy portion of each tubular strut is $-0.37 \times 10^{-6}/^{\circ}\text{F}$; thus, the thermal expansion of the truss is largely driven by the high CTE (about $13.0 \times 10^{-6}/^{\circ}\text{F}$) of the aluminum-joint hardware.

Because the surface-accuracy results shown in figure 20 were obtained by comparing (through a best-fit computation) photogrammetric data to analytically predicted truss shapes, a natural question arises about the sensitivity of the surface-accuracy results to inaccuracies in the analytical model. Inaccuracies in the analytical model result in errors in the predicted target locations, and thus degrade the rms best fit with the experimentally measured target locations. This question was investigated by varying two of the analysis input parameters—the strut modulus E and the temperature difference ΔT between the as-fabricated and as-measured truss.

The effect of varying these model input parameters on computed rms surface accuracy is shown in figure 22 for photogrammetric survey 1 (Test temperature = 72.6°F). The figure shows the sensitivity of the grand rms difference between measured and predicted target coordinates to changes in model input values for E and ΔT . The nominal input values are 16.9×10^6 psi for E and 3.6°F for ΔT (obtained by subtracting the strut

fabrication temperature of 69°F from the test temperature of 72.6°F). Figure 22 indicates that the rms difference is relatively insensitive to changes in the input modulus. For example, if the input strut modulus used for analysis is reduced to 60 percent of the nominal value, the computed grand rms difference decreases by only 1.8 percent (from about 0.00280 in. to about 0.00275 in.). The rms difference is slightly more sensitive to the assumed temperature difference ΔT . For example, reducing the input value of ΔT from 3.6°F to 2.2°F (a reduction of 40 percent) increases the grand rms difference by 6.7 percent (from 0.0028 in. to 0.0030 in.). Therefore, errors in the assumed values for E and ΔT (or strut CTE) are not the primary factors responsible for the rms differences shown in figure 20.

Concluding Remarks

Test procedures and experimental results that characterize a first-generation, doubly curved support truss for precision reflector applications have been described. Static, dynamic, and surface-accuracy test results have been presented.

The static-test results were in good agreement with analytical predictions. The load-displacement response of the truss was predictable and nearly linear. The load-strain response of the truss struts was also predictable and repeatable. Although the strain response data exhibited some nonlinearity, the results verified basic structural performance and were reasonable, considering the low strain magnitudes that were measured. Static-test results for the truss with six struts removed were also in generally good agreement with analysis, but were not as predictable as for the complete truss. The static-test displacement results were biased by motion of the support table on which the truss was mounted. All static-test results were also in good agreement with results presented in reference 1; thus, the repeatability of the test measurements was demonstrated.

Dynamic test results correlated well with analysis and demonstrated repeatability. The results verified that an unpredicted mode observed during initial testing (and first reported in ref. 1) was caused by the flexibility of the truss support system. Experimentally determined frequencies and mode shapes agreed well with analytical predictions for both fixed and approximate free-free support conditions. As expected, the truss exhibited a low level of modal damping.

The results of two photogrammetric surveys (surveys 2 and 3) indicated that the grand truss root-mean-square (rms) surface error is approximately 0.0025 in. This is about 10 percent smaller than the error determined previously (survey 1) and reported in

reference 1. The results of all three surveys show that the grand rms surface error is well within the design goal of 0.004 in. for the Precision Segmented Reflector program. Based on the results of the surface-accuracy surveys, the thermal expansion of the truss was consistent with the coefficient of thermal expansion that was predicted by analysis. It was also shown that the surface-accuracy results that were obtained by comparing analytical and experimental results are relatively insensitive to analysis input parameters.

The experience gained from testing the truss yielded several valuable lessons for the testing of future structures. For example, a stable foundation is extremely important for both static and dynamic testing. Although the support table weighed 13000 lb, it was not completely restrained. As a result, the response of the support table influenced both the static and dynamic test results. Results of initial dynamic testing (in which an unpredicted mode was observed) emphasize the need for truss support fixtures whose behavior can be predicted accurately. If extreme accuracy is needed, either detailed modeling of the support fixtures or complete testing of the truss in a better approximated free-free configuration may be required.

Photogrammetry is a valuable method for determining truss-surface accuracy. However, for high precision, the photogrammetric procedure requires the application of many reflective targets whose positions relative to the truss surface must be known with great accuracy. The design and fabrication of target holders that will place the target centers at precisely known X, Y, and Z coordinates represent special challenges. The thickness and eccentricity of the targets themselves, and perhaps even the thickness of the masking material used to delineate the target boundaries, must be taken into account to predict measured target locations with the desired precision. Also, the photogrammetric results are very sensitive to the independently determined lengths of the reference scales. To determine rms surface errors of a few thousandths of an inch, it is necessary to determine the length of each reference scale with similar precision. Because of the length of the scaling tubes (about 11 ft), such precise measurements are difficult. This challenge is even greater for larger truss structures because they require even longer reference scales.

These challenges aside, testing and analysis of the truss demonstrated a first-generation erectable truss structure that exhibits linear and predictable structural performance. Surface-accuracy measurements verified the feasibility of such a structure for precision reflector applications.

Appendix

Details of Photogrammetric Measurements

Convergent close-range photogrammetry was used to measure the three-dimensional coordinates of a set of high-contrast targets located on the upper-surface nodes of the test-bed truss for the Precision Segmented Reflector program. The data were obtained from full-coverage metric-camera photographs of the target field taken from 24 different vantage points above the truss. The hardware and software used for the planning, execution, and analysis of the photographs are incorporated in a turnkey photogrammetric system known as the Simultaneous Triangulation and Resection System (STARS), a series of products developed and licensed by Geodetic Services, Inc. (GSI).

A brief overview of the photogrammetric principles involved in these measurements is included in this appendix. For a more rigorous discussion of the theory, equations, hardware, and software of STARS, see references 5 and 6.

All photogrammetry is based on a simple pair of equations, herein called the projective equations. These equations relate the two-dimensional, as-measured, x - y coordinates of the target images to the corresponding three-dimensional object-space coordinates (X , Y , Z) of the actual targets. This relationship is expressed in terms of several constants, often referred to as the projective parameters. The projective equations are derived from geometrical optics on the basis of the fundamental assumptions that all target images lie in a common image plane, and that the photographed target in object space, its image, and the center of projection of the lens lie on a common straight line.

For the case of a multistation, single-camera network, the projective parameters for each station include the X , Y , Z coordinates of the center of projection in object space and the three rotation angles that define the orientation of the axes of image space with respect to those of object space. The projective parameters for the camera include the three coordinates of the center of projection in image space. Lens distortions, while considered as systematic errors, are dependent upon the target distances from the camera; therefore, they are best modeled as parameters to be solved for in the projective equations. Thus, five lens-distortion coefficients (three radial and two decentering) are carried in the STARS adjustment as additional parameters to effect camera self-calibration.

A pair of projective equations is generated for each target image on each photograph. Therefore, if the image

coordinates x, y for each of n targets are measured on each of m photographs, a system of $2mn$ projective equations results. Besides the $3n$ unknowns (X , Y , Z) for the object-space coordinates of the targets, the projective equations carry as unknowns the $6m$ station parameters, the 3 camera parameters, and the 5 additional parameters to account for lens distortions.

Network Simulation

The STARS computer simulations were used to plan the photogrammetric network that was required to achieve the desired measurement precision. Sound photogrammetric design practice suggests that the ratio of measurement precision to hardware tolerance be at least 1:5, and preferably 1:10, to accommodate statistical fluctuations in the measurement results. The design tolerance for the truss components was assumed to be better than 1 mil, and the anticipated assembly tolerance for the 27 upper-surface node centers was expected to be on the order of 3 mils. Therefore, a network measurement precision goal of 0.0003 in. to 0.0006 in. was desired. The STARS computer simulations predicted that this measurement precision could be attained by using 24 equally spaced camera stations that were located on a circle centered 13 ft above the truss center. Sufficient data to assure camera self-calibration could be attained by incrementing the lens roll angle 45° for each camera station. Predicted precisions for the recovery of camera and station parameters, and for the recovered target coordinates, were used to develop the complete plan for conduct of the measurements.

Targets

Threaded target mounts were installed in the 27 upper-surface nodes. Disks of retroreflective tape were affixed to the top of each target mount. The mounts, when threaded into the nodes, were designed to center by virtue of their machined shoulders and to seat squarely on the flat of the node when tightened. Prior to the photography, 24 additional secondary targets were placed below the truss on the upper surface of the support plate to provide the required geometric depth for strengthening the recovery of projective parameters during the photogrammetric analysis of the data.

Photography

Metric photography was accomplished by using a large-format metric camera fitted with a 240-mm lens cone focused to a distance of 119.4 ft at an aperture of $f/32$. The camera was mounted on a heavy-duty pan-tilt tripod that was securely fastened to the platform safety railing of the high-lift device (fig. 19). The ability to

rotate the truss greatly simplified the metric-photography procedure by eliminating the need to drive the high-lift device around the truss for the required views.

A series of full-coverage metric photographs of the truss were taken with the camera at a horizontal distance of 12 ft from the truss center of rotation. Two photographs were taken at each of the 24 camera stations. A shutter speed of 1/125 sec was used to expose the background-suppressed photograph, and the orientation photograph was exposed for 10 sec.

For all photographs, retrotarget illumination was provided by a 200 W-sec battery-powered strobe lamp mounted to the camera at a distance of 10 in. from the lens. The truss was rotated in 15° increments about its vertical axis to provide a different view to the camera for each station-photograph pair. Also, the camera was rolled 45° about the lens axis to allow for camera self-calibration during analysis of the data.

Film Reading

After the film was processed, the x - y coordinates of each target on each side of the data photographs were measured to a precision of 0.5 μ m by using an Autoset monocomparator. For the first measurement, this was accomplished in two stages. First, the targets from four stations separated by 90° were read in the semiautomatic mode. These data were then merged and, by using the design coordinates of the top nodes as control, a preliminary resection was completed to recover improved estimates of the station parameters for each of the four selected stations. The initial three-dimensional coordinates for each target were then generated by a preliminary triangulation. The second stage utilized the automatic-resection-driveback feature of Autoset to complete observation of the remaining data frames. The image coordinates for each data frame were preprocessed to correct for systematic errors that were introduced by film distortion and the calibration function of the Autoset comparator. For the succeeding measurements, film observations were made by using the Autoset automatic-resection-driveback mode only, since approximate coordinates for all targets were known from the first measurement.

Data Analysis

Three sets of measurements were made on the truss at Langley Research Center. The objective of test 1 was to compare the shape of the as-assembled structure with its predicted shape. Tests 2 and 3 were conducted to repeat test 1 with two longer and more precisely measured reference scales and to assess the effect of tempera-

ture on the shape and size of the truss. For all three measurements, a free-network iterative, least-squares bundle adjustment with self-calibration was performed on the data by using the STARS photogrammetric software. In the free-network adjustment, the object-space coordinate-system is not explicitly defined by using control targets, but is iteratively established as a result of the adjustment so as to generate the covariance matrix of the entire set of triangulated coordinates with a minimum trace (sum of diagonal elements). In this sense, the coordinate-system is defined implicitly to produce results with the highest possible overall accuracy. Accordingly, all points participate equally in the definition of an object-space coordinate-system to preserve the mean position, mean orientation, and mean scale of the network with respect to the approximate starting values that are adopted for the coordinates of the targets. In essence, the least-squares bundle adjustment adds seven additional parameters, which define a unique scaled object-space coordinate-system, to the number of unknowns that are carried in the projective equations.

The data for each measurement thus consisted of a system of $2mn$ projective equations to solve for $3n + 6m + 3$ projective parameters and 12 additional parameters. Since there were 24 stations ($m = 24$) used to measure 60 targets ($n = 60$), a total of 2880 equations were generated with only 339 unknowns. The STARS bundle-adjustment software exploits this overdetermination by using the method of least squares to extract from the entire set of projective equations a reduced set of equations (the normal equations) that lead to results with the greatest possible accuracy. While the unknown parameters are determined from the solution of the normal equations, the square roots of the diagonal elements of the inverse of the coefficient matrix of the normal equations provide the corresponding standard errors.

Photogrammetric Results

Free-network adjustment results, while approximating the sense and scale of the preferred coordinate-system, are obtained in an arbitrary coordinate system. Thus, to compare the measurement results with analytical predictions, a coordinate-system transformation is first required. The STARS rigid-body transformation module was used for this task. This transformation software is used to perform the required translations, rotations, and scaling (if desired) to best overlay, in a least-squares sense, the photogrammetric results with analytical predictions.

Independent scaling of each measurement was provided by including calibrated reference scales in the

camera field of view. For the first measurement (survey 1, ref. 1), a single 1-in-diameter graphite-epoxy tube, approximately 6 ft long and with retrotargets placed near each end, was taped to the upper surface of the truss to serve as a reference scale. For surveys 2 and 3, two scales, approximately 11 ft in length, were used. These longer scales were mounted to the truss support plate on standards to raise them slightly above the truss upper surface. They were targeted along their length and crossed at an angle, one just above the other. The purpose of using two scales was to strengthen the statistical reliability of the scaling of the photogrammetric measurements.

Inclusion of the calibrated distances between scaling targets into the STARS bundle adjustment resulted in sizing of the results for all measurements. Subsequent coordinate transformation allowed only three translations and three rotations of the measurement data; the scale was not allowed to adjust. For surveys 2 and 3, the scaling distances were corrected for test temperature by using the measured coefficient of thermal expansion of the graphite-epoxy reference scales. The 1- σ rms precision for upper-surface and scaling targets was 0.0002 in. in X and Y and 0.0003 in. in Z in all three surveys. This precision corresponds to a proportional accuracy of about one part in 600000 of the truss diameter.

References

1. Bush, Harold G.; Herstrom, Catherine L.; Heard, Walter L., Jr.; Collins, Timothy J.; Fichter, W. B.; Wallsom, Richard E.; and Phelps, James E.: Design and Fabrication of an Erectable Truss for Precision Segmented Reflector Application. *J. Spacecr. & Rockets*, vol. 28, no. 2, Mar.–Apr. 1991, pp. 251–257.
2. Umland, J.; and Lou, M.: Precision Segmented Reflector Primary Support Structural Testing. AIAA-92-2535, Apr. 1992.
3. Collins, Timothy J.; and Fichter, W. B.: *Support Trusses for Large Precision Segmented Reflectors: Preliminary Design and Analysis*. NASA TM-101560, 1989.
4. *I-DEAS Master Series™—I-DEAS Test™ User's Guide, Volume 1*. Struct. Dyn. Res. Corp., 1994.
5. Brown, Duane C.: *Application of Close-Range Photogrammetry to Measurements of Structures in Orbit*, Volume 1. GSI Tech. Rep. No. 80-012 (Contract No. MOM7DNS-895942), Geodetic Services Inc., Sept. 15, 1980.
6. Slama, Chester C., ed.: *Manual of Photogrammetry*. Fourth ed., American Soc. of Photogrammetry, 1980.

Table 1. Summary of Truss Structural Tests

Static load	Vibration	Surface accuracy
^a Vertical nodal displacements (10 node locations)	^a Normal modes and frequencies (truss supported at three nodes)	^a Photogrammetry survey (one reference scale; $T = 72.6^{\circ}\text{F}$)
Vertical nodal displacements (18 node locations)	Normal modes and frequencies (with redesigned support fixtures)	Photogrammetry surveys (two reference scales; $T = 77.5^{\circ}\text{F}$ and 63.0°F)
Axial strut strain (27 locations)	Approximated free-free vibration	
Displacements and axial strains (selected truss members removed)		

^aResults of these tests presented in reference 1.

Table 2. Truss Component Properties

(a) T300/5208 graphite-epoxy tube

Outer diameter, in.	1.0
Wall thickness, in.	0.0624
Density, lbm/in ³	0.0576
Extensional modulus, psi	16.9×10^6
Coefficient of thermal expansion, per deg F	-0.369×10^{-6}

(b) 7075 aluminum joint node

Joint mass, lbm.	0.4321
Node mass, lbm	0.2405
Joint length, in.	13.094
Extensional stiffness (Modulus \times Area), lbf	1.9×10^6
Coefficient of thermal expansion, per deg F	13.0×10^{-6}

Table 3. Analysis and Dynamic Test 1

(a) Results

Mode	Analysis frequency, Hz (a)	Test 1 frequency, Hz	Test 1 damping (percent of critical)	MAC (test 1 analysis)	Description
1	35.04	34.5	1.35	0.96	Rocking
2	35.05	35.6	1.19	0.95	Rocking
3	(b)	51.9	1.73	(b)	(b)
4	59.73	57.3	1.45	0.98	Torsion
5	73.31	78.1	1.15	0.98	Umbrella
6	92.26	96.6	0.97	0.83	Saddle
7	92.33	97.3	1.11	0.62	Saddle
8	120.84	123.7	1.01	0.94	Radial flutes
9	125.75	129.0	0.89	0.85	Rocking and truss bending
10	126.90	130.1	0.84	0.87	Rocking and truss bending

^aAnalysis frequencies obtained by using refined analysis model with strut bending effects (ref. 1).

^bNot predicted by finite-element model.

(b) Mode shapes


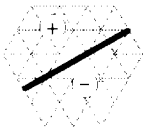
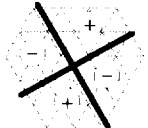


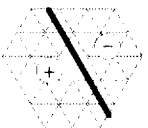

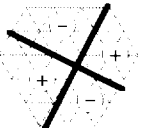
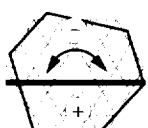



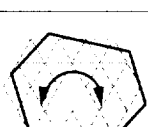

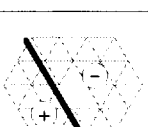
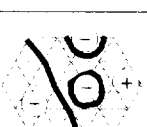
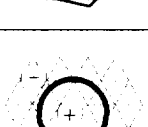
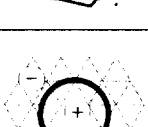

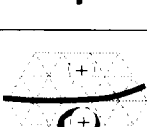
Mode	Test 1	Analysis	Mode	Test 1	Analysis
1			6		
2			7		
3			8		
4			9		
5			10		

Table 4. Analysis and Dynamic Test-2 Results

Mode	Analysis frequency, Hz (a)	Test 2 frequency, Hz	Test 2 damping (percent of critical)	MAC (test 2 analysis)	Description
1	35.04	36.4	1.06	1.00	Rocking
2	35.05	37.3	1.08	1.00	Rocking
3	59.73	64.5	0.99	0.99	Torsion
4	73.31	80.1	1.09	1.00	Umbrella
5	92.26	96.6	0.97	0.98	Saddle
6	92.33	96.8	0.98	0.99	Saddle
7	120.84	124.0	0.98	1.00	Radial flutes
8	125.75	133.4	0.89	0.90	Rocking and truss bending
9	126.90	136.5	0.90	0.63	Rocking and truss bending

^aAnalysis frequencies obtained by using refined analysis model with strut bending effects (ref. 1).

Table 5. Natural Frequencies for Analysis, Test 1, and Test 2 Results

Mode	Analysis frequency, Hz (a)	Test 1 frequency, Hz	Test 2 frequency, Hz
1	35.04	34.5	36.4
2	35.05	35.6	37.3
3	59.73	57.3	64.5
4	73.31	78.1	80.1
5	92.26	96.6	96.6
6	92.33	97.3	96.8
7	120.84	123.7	124.0
8	125.75	129.0	133.6
9	126.90	130.1	136.5

^aAnalysis frequencies obtained by using refined analysis model with strut bending effects (ref. 1).

Table 6. Analysis and Dynamic Test Results for Approximate Free-Free Truss Configuration

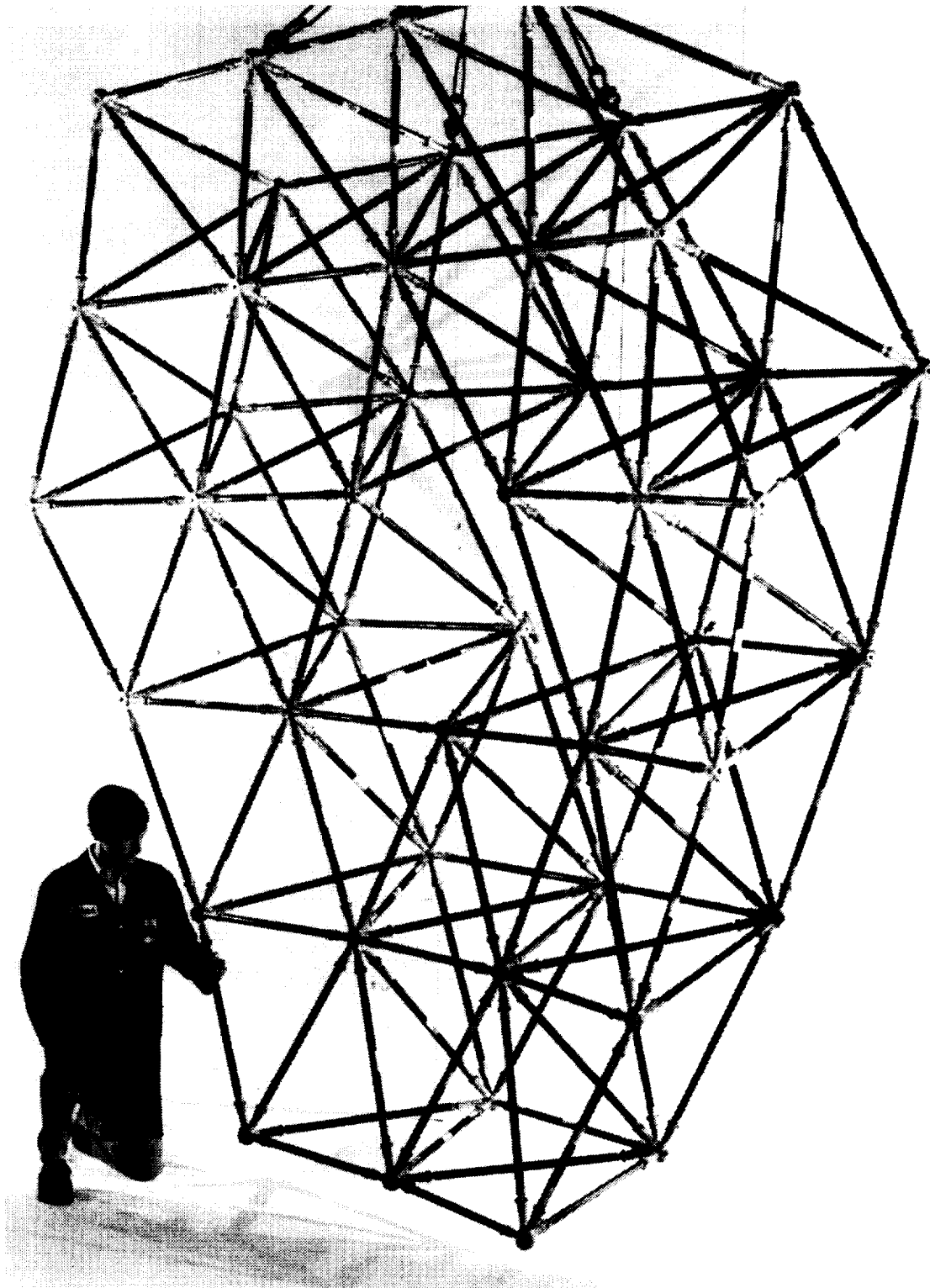
Mode	Analysis frequency, Hz (a)	Test frequency, Hz	Test damping (percent of critical)	MAC (test analysis)
1	82.1	86.0	1.18	0.93
2	82.1	87.4	0.94	0.92
3	123.6	122.2	1.10	1.00
4	125.0	123.4	1.20	0.96

^aAnalysis frequencies obtained by using simplified analysis model with no strut bending effects (ref. 1).



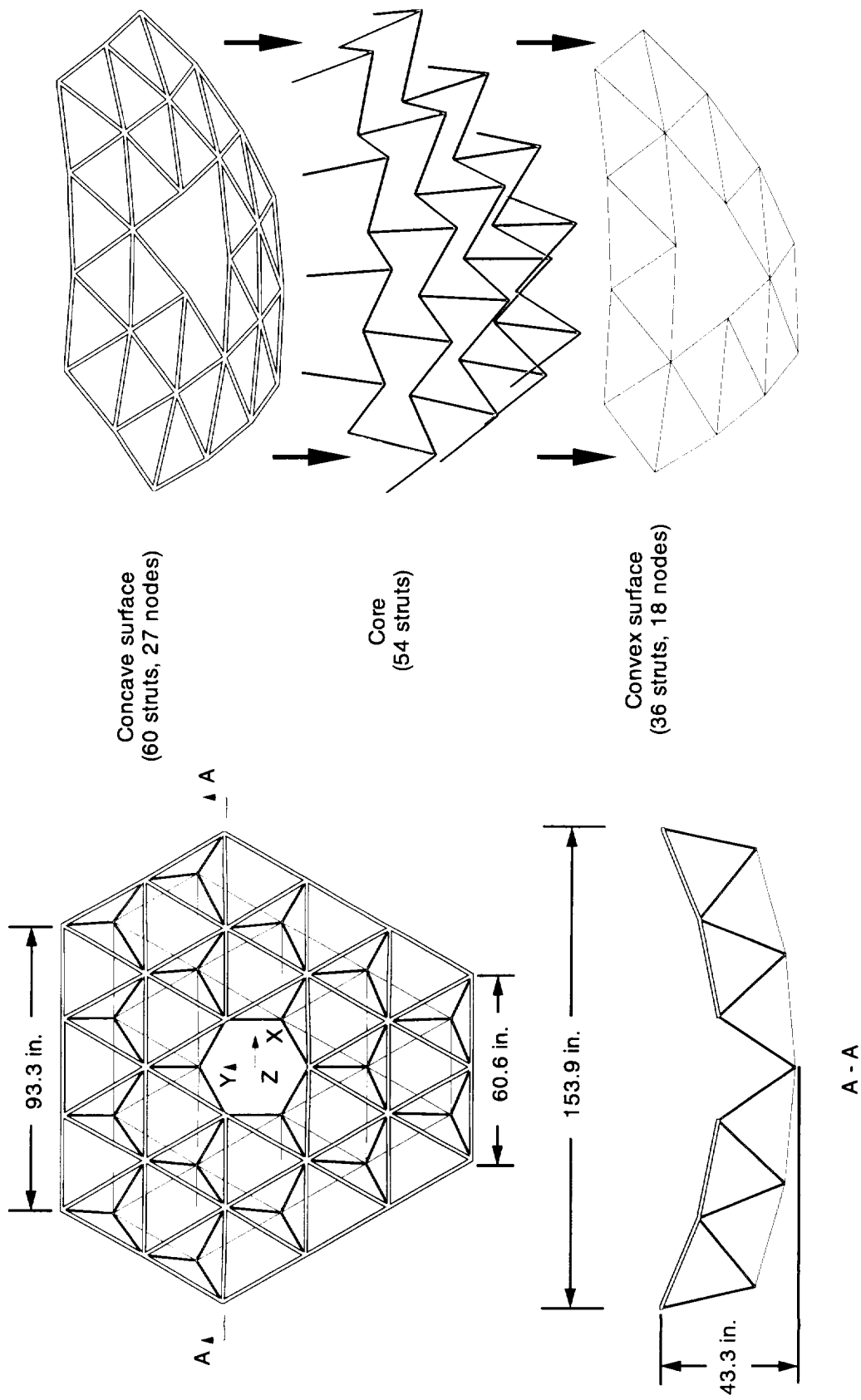
L-90-15358

Figure 1. Submillimeter astronomical observatory.



(a) Photograph.

Figure 2. Erectable PSR truss.



(b) Schematic.

Figure 2. Concluded.

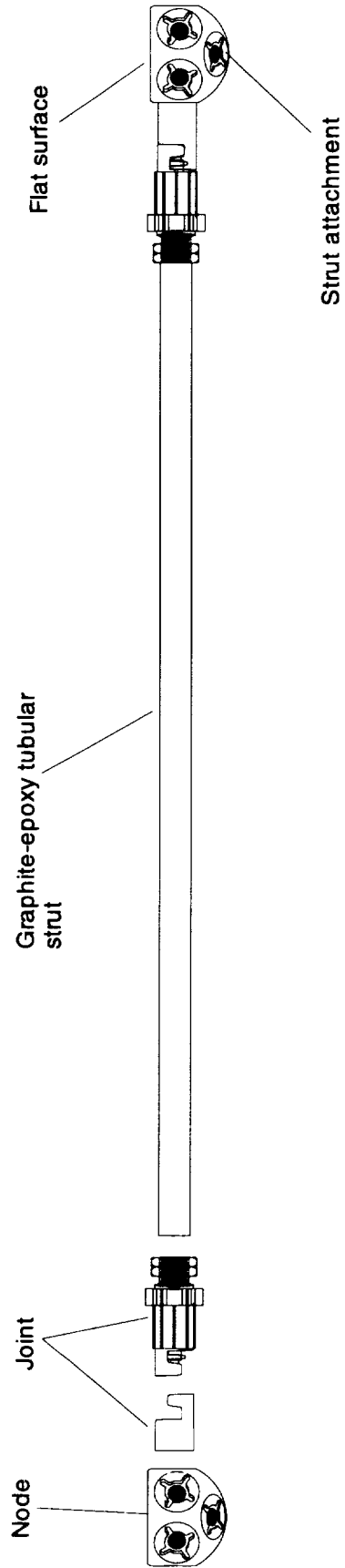


Figure 3. Configuration of strut, nodes, and joints in a typical strut assembly.

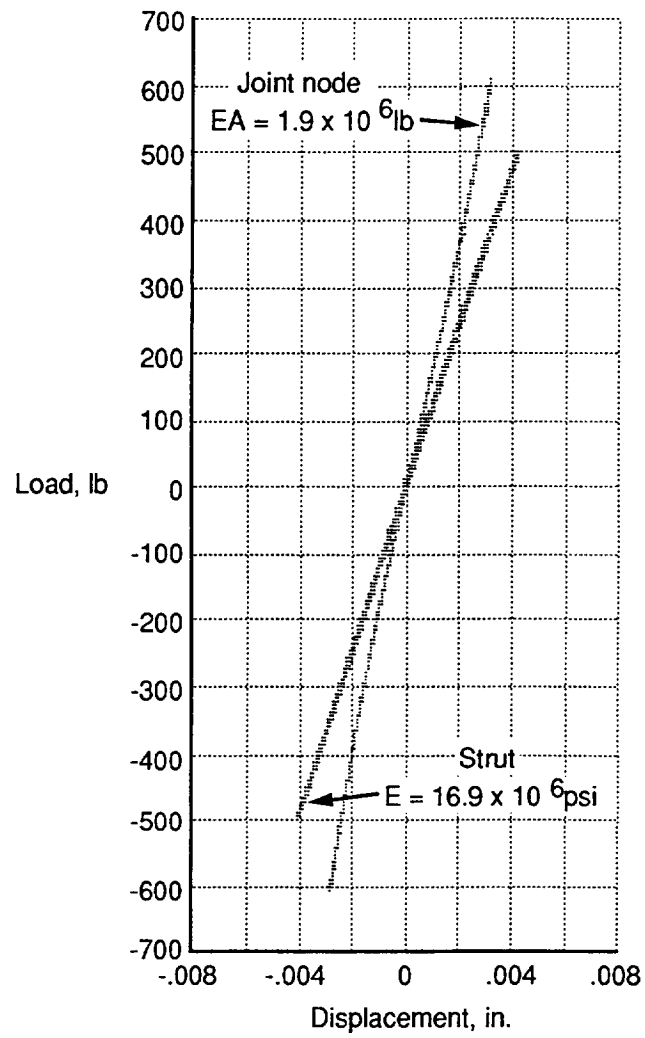
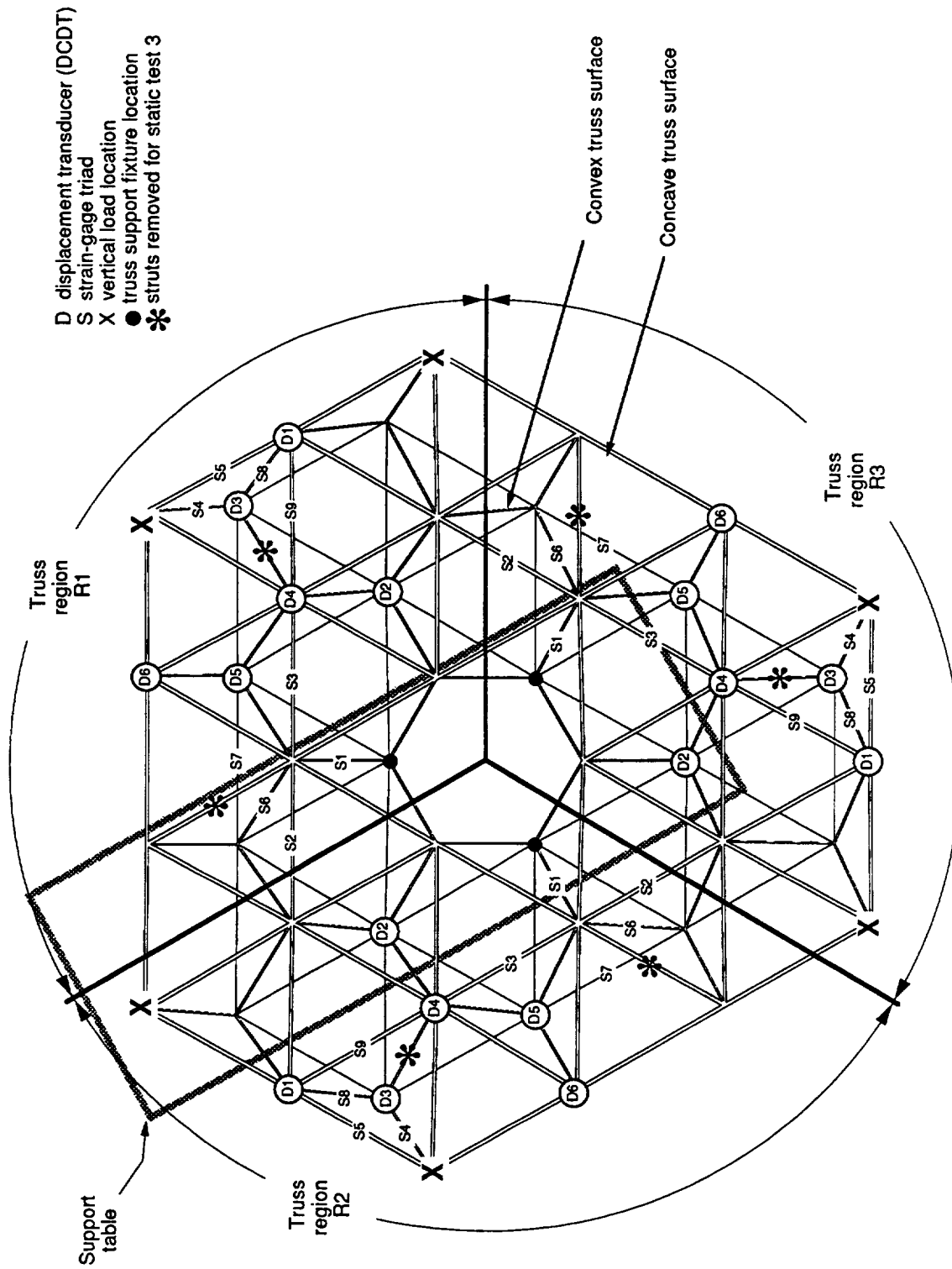
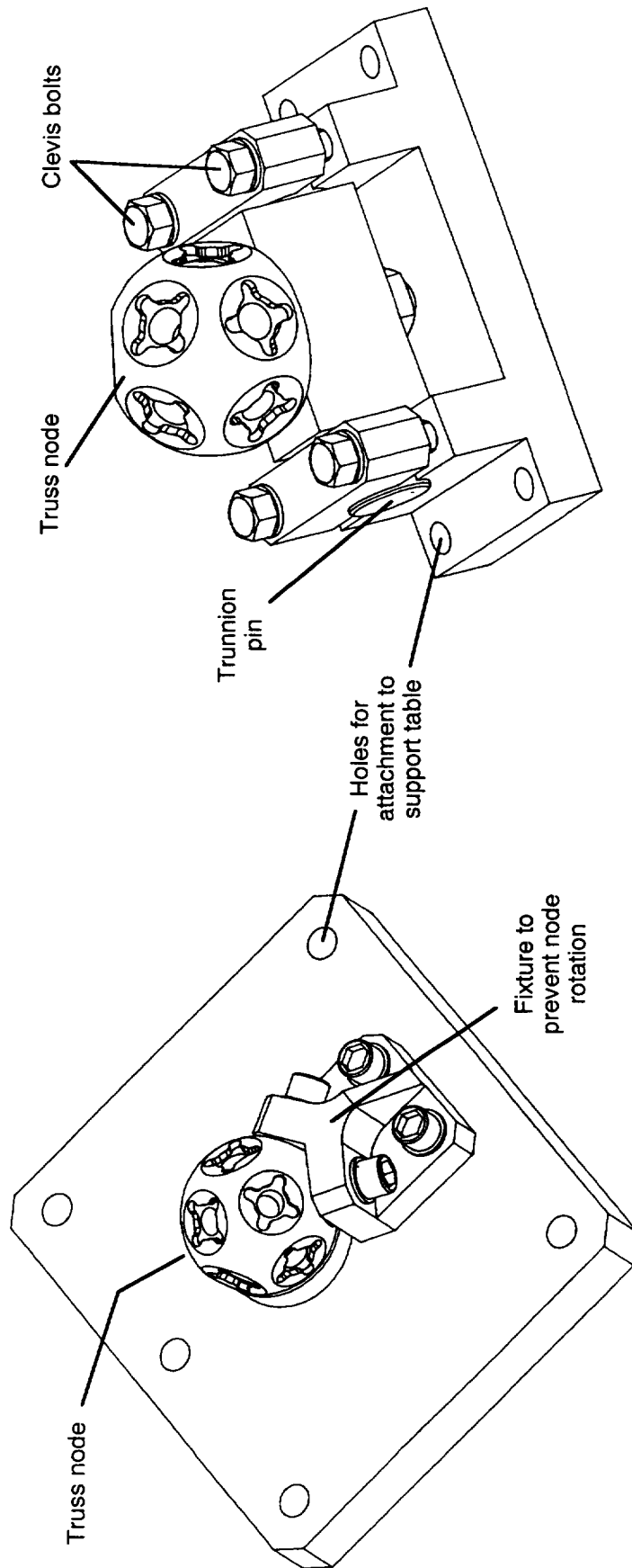


Figure 4. Load-displacement test results for a typical strut and joint-node combination.

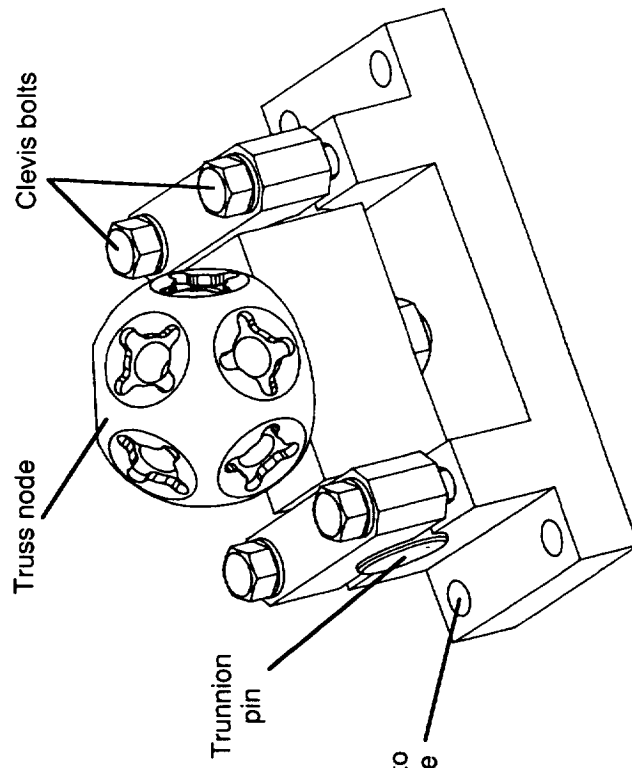


(a) Truss setup.

Figure 5. Truss static test setup and support fixtures.



(b) Typical fixed support fixture.



(c) Typical trunnion support fixture.

Figure 5. Concluded

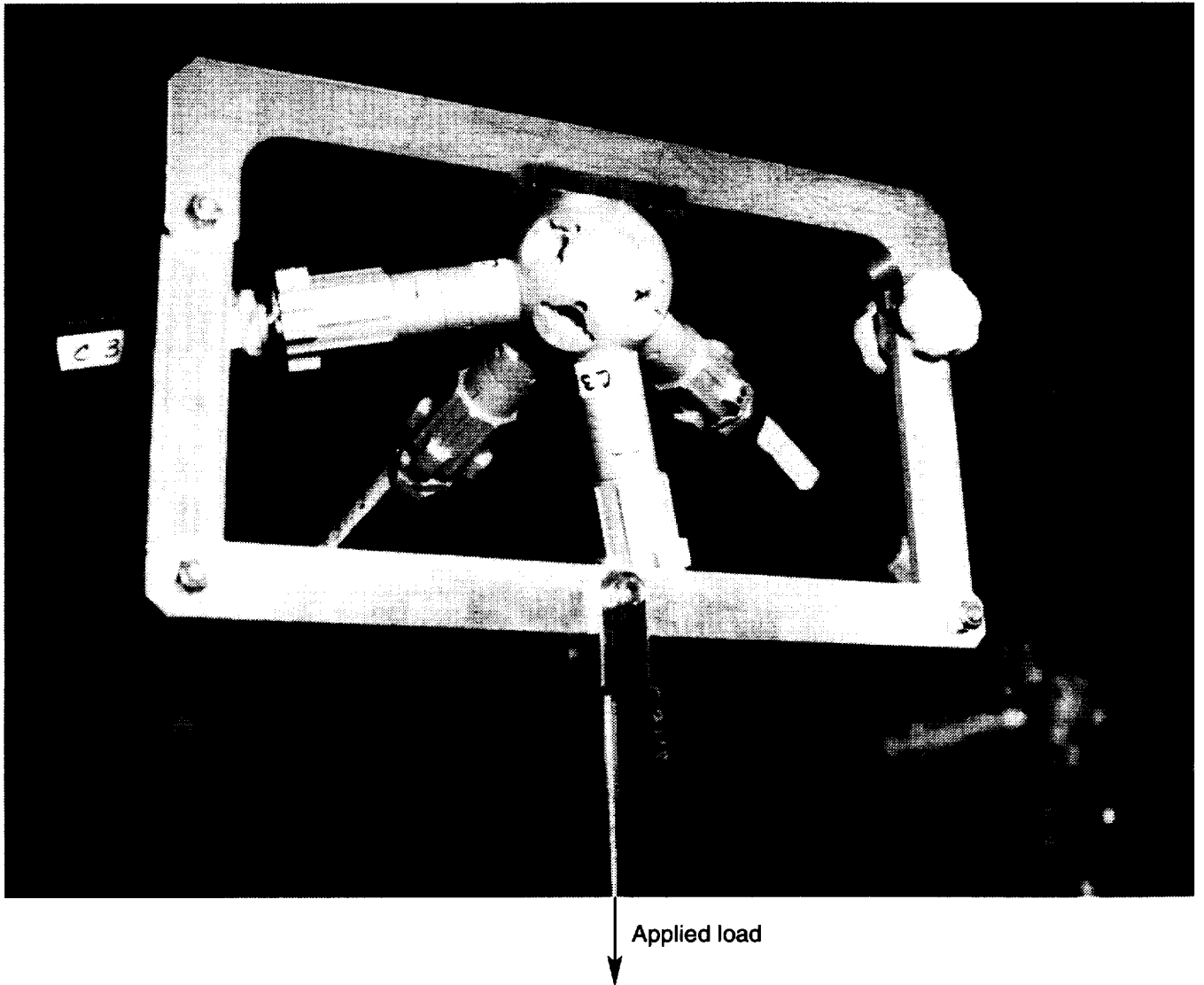
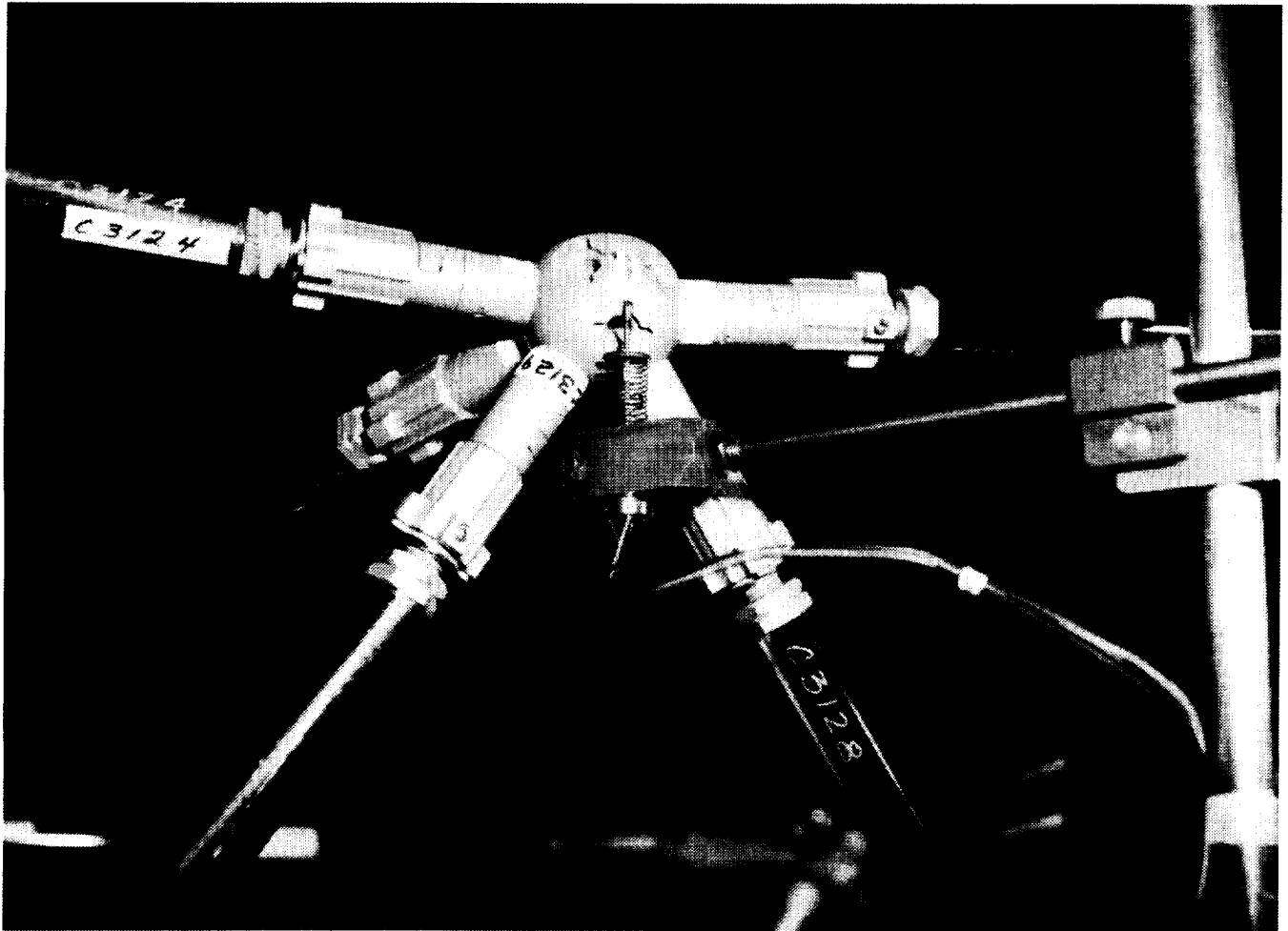


Figure 6. One of six weight hangers used to apply vertical loading.

L-89-13230



L-89-13233

Figure 7. Direct-current displacement transducer (DCDT) used to measure vertical node displacement.

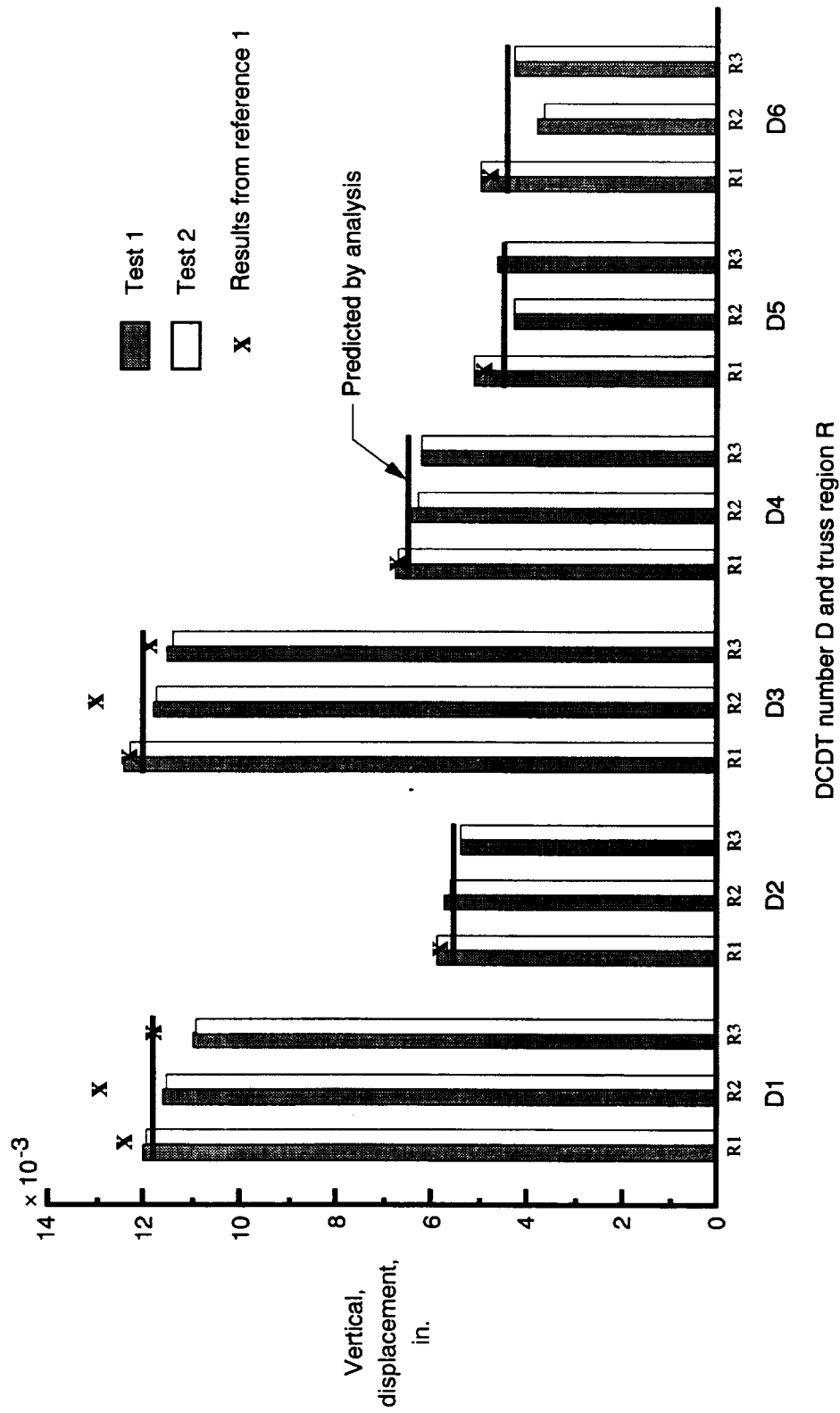


Figure 8. Comparison of measured and predicted nodal displacements at maximum load (tests 1 and 2).

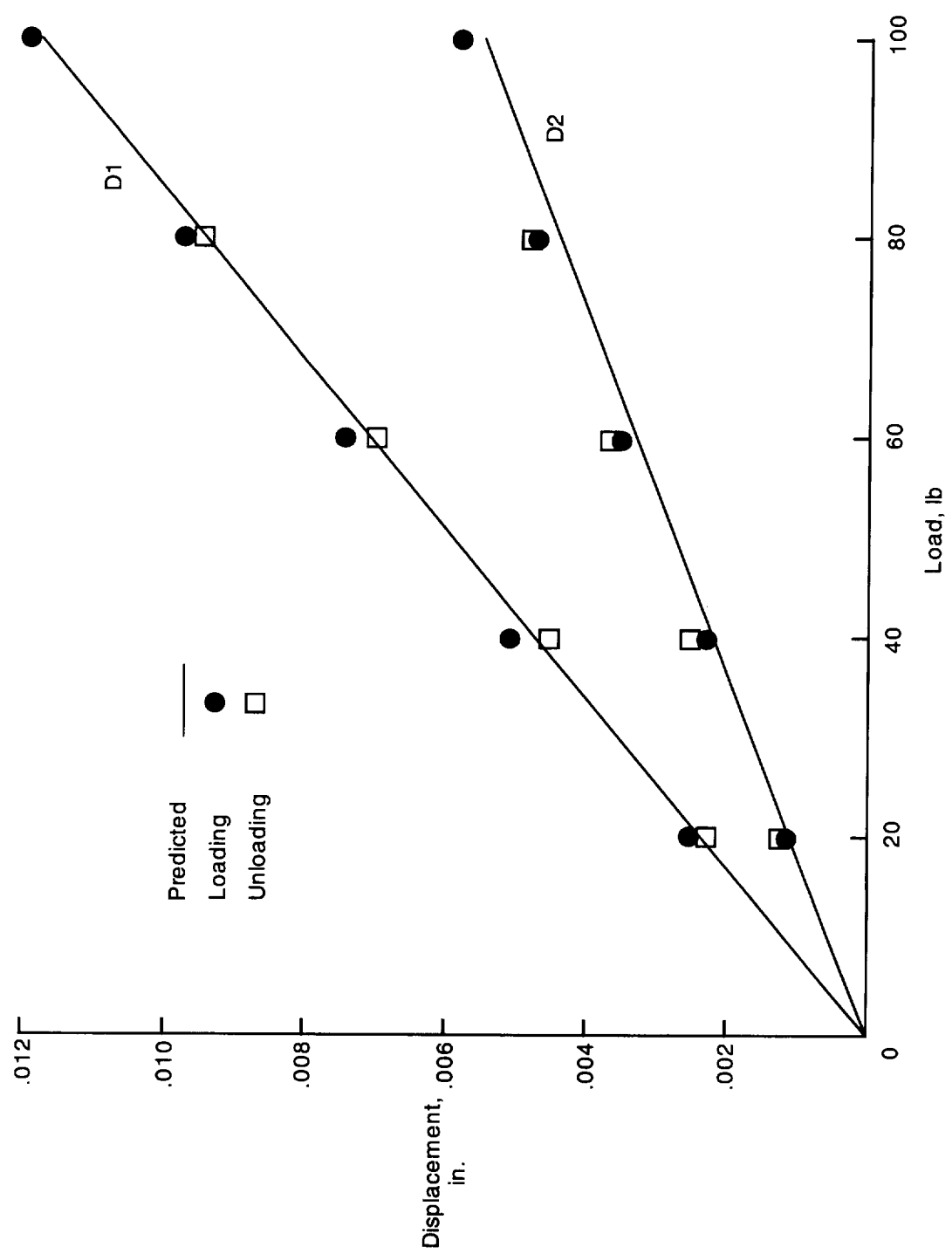


Figure 9. Typical plots of nodal displacement as a function of load (test 1, truss region 1).

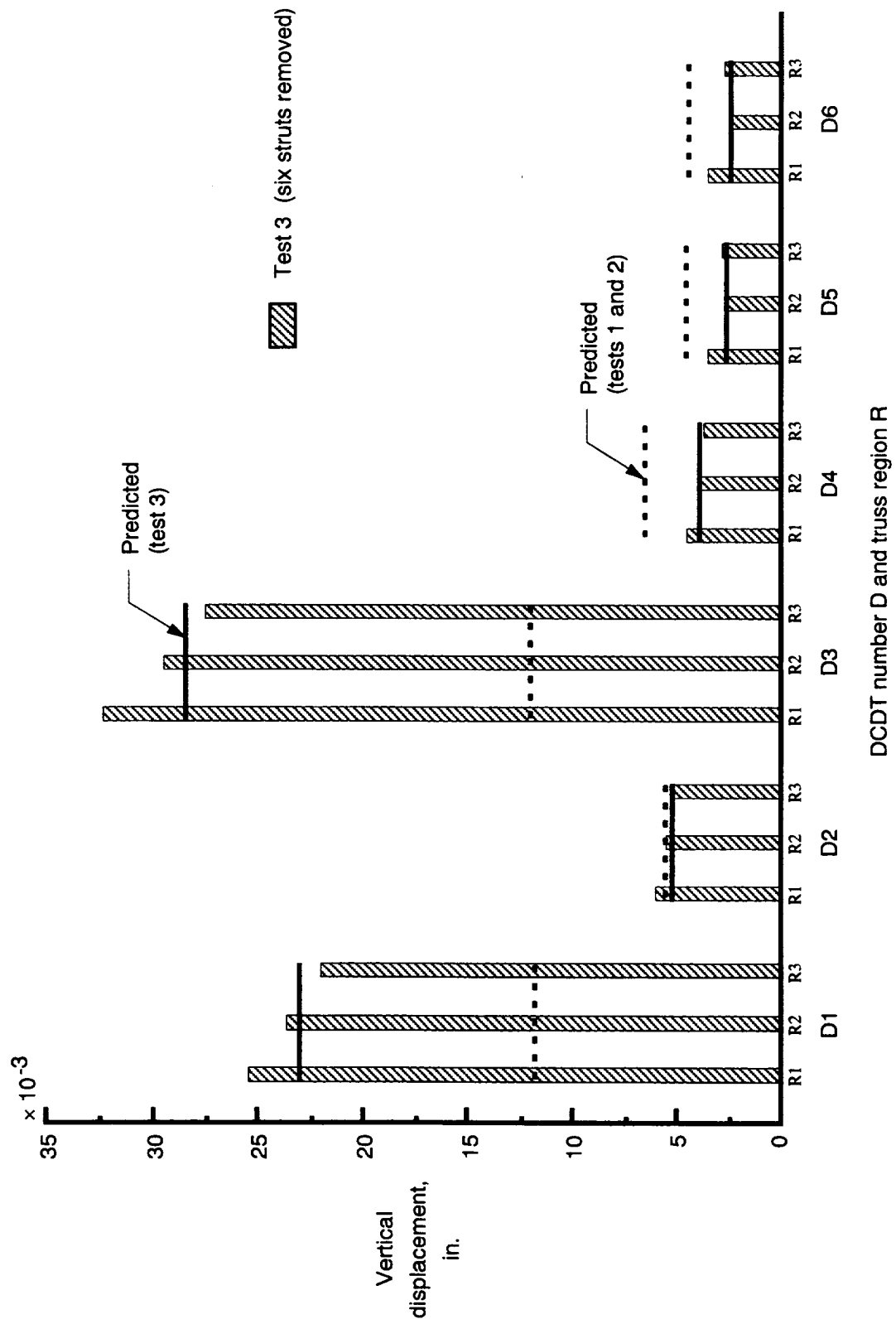


Figure 10. Comparison of measured and predicted nodal displacements at maximum load with six struts removed (test 3, see fig. 5).

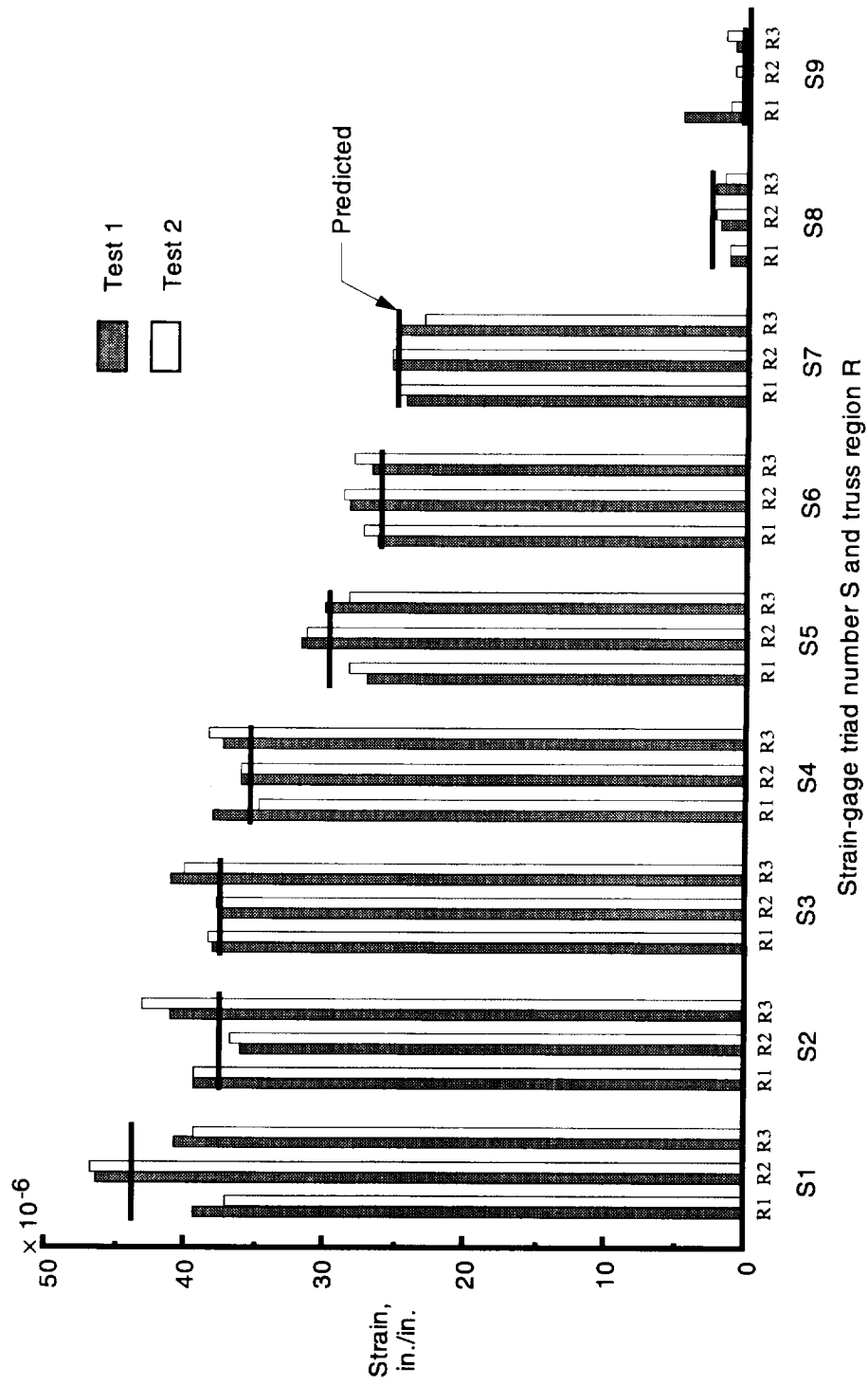


Figure 11. Comparison of measured and predicted strain magnitudes at maximum load (tests 1 and 2).

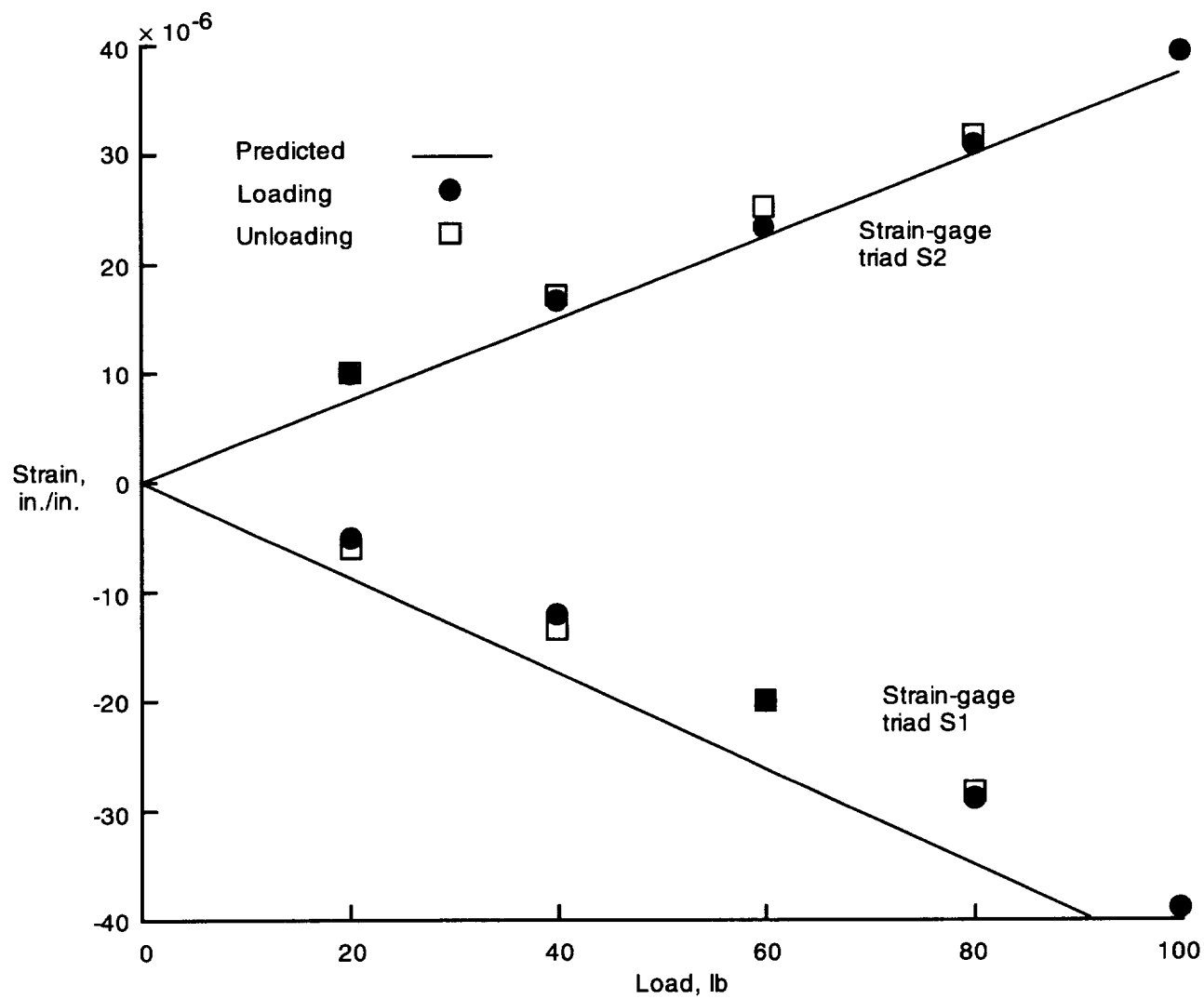


Figure 12. Typical plots of axial strain as a function of vertical load (test 1, truss region 1).

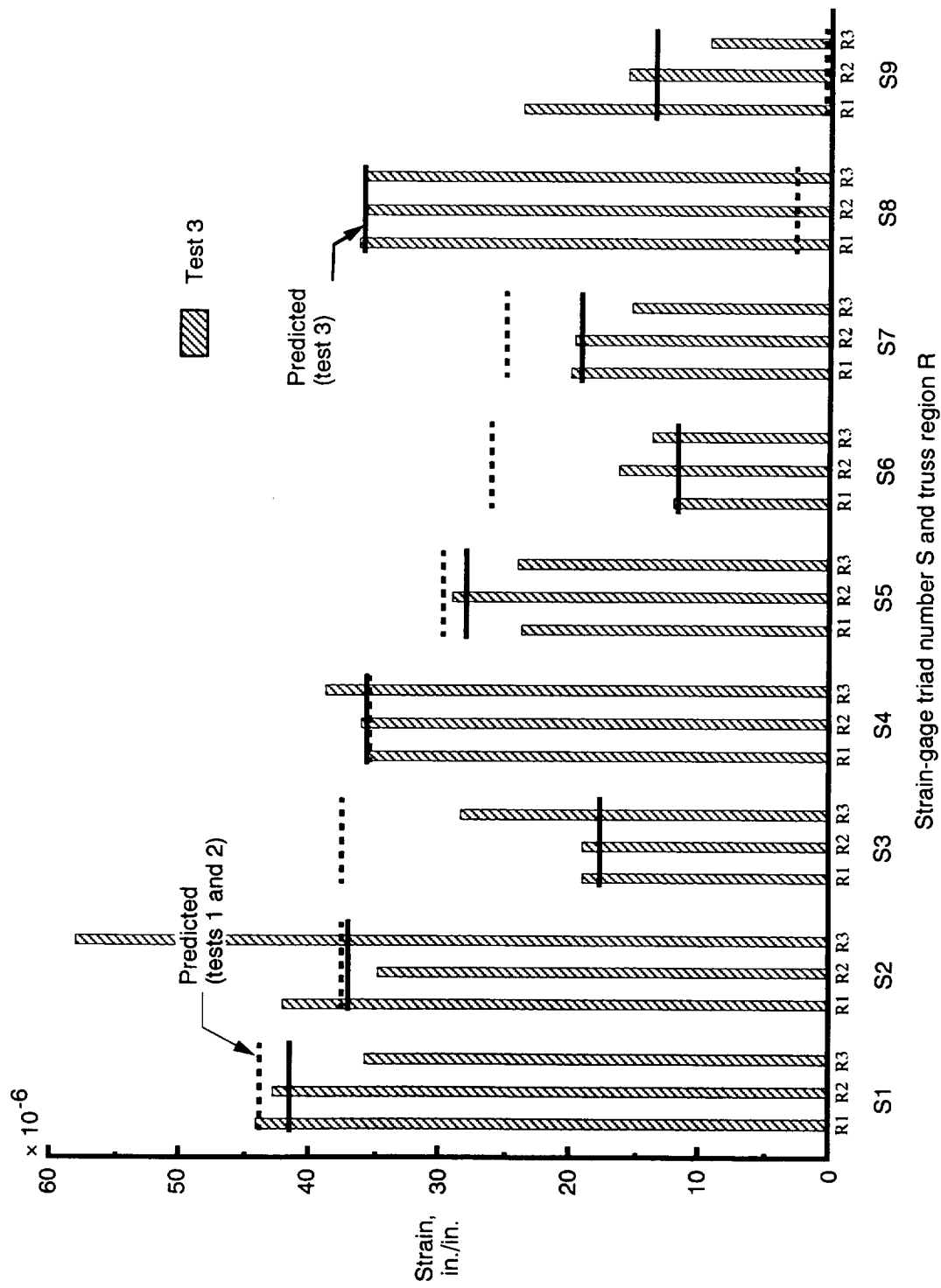


Figure 13. Comparison of measured and predicted strain magnitudes at maximum load and with six struts removed (test 3, see fig. 5(a)).

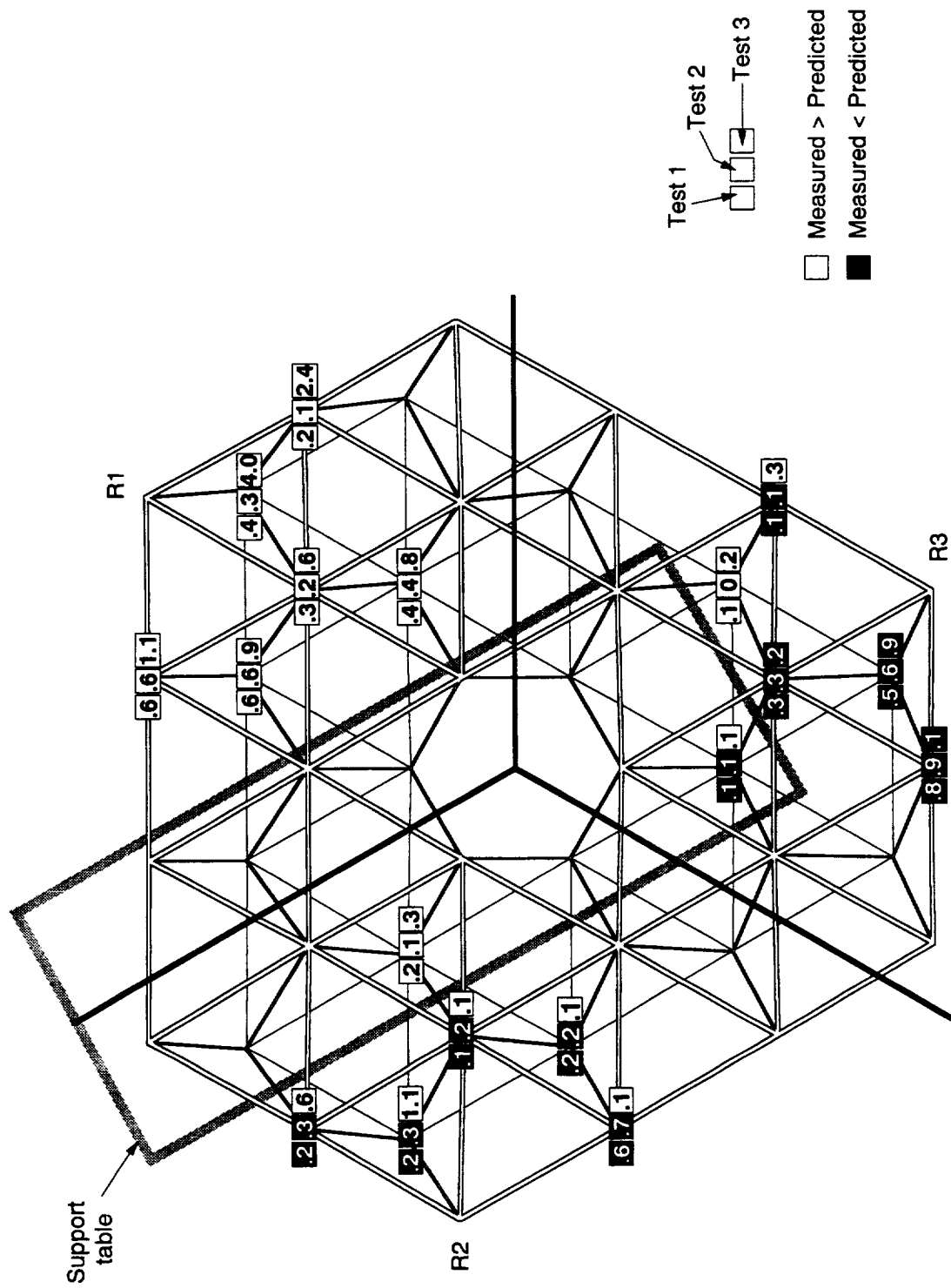


Figure 14. Differences between measured and predicted displacements for static tests 1, 2, and 3. Differences are in inches and should be multiplied by 10^{-3} .

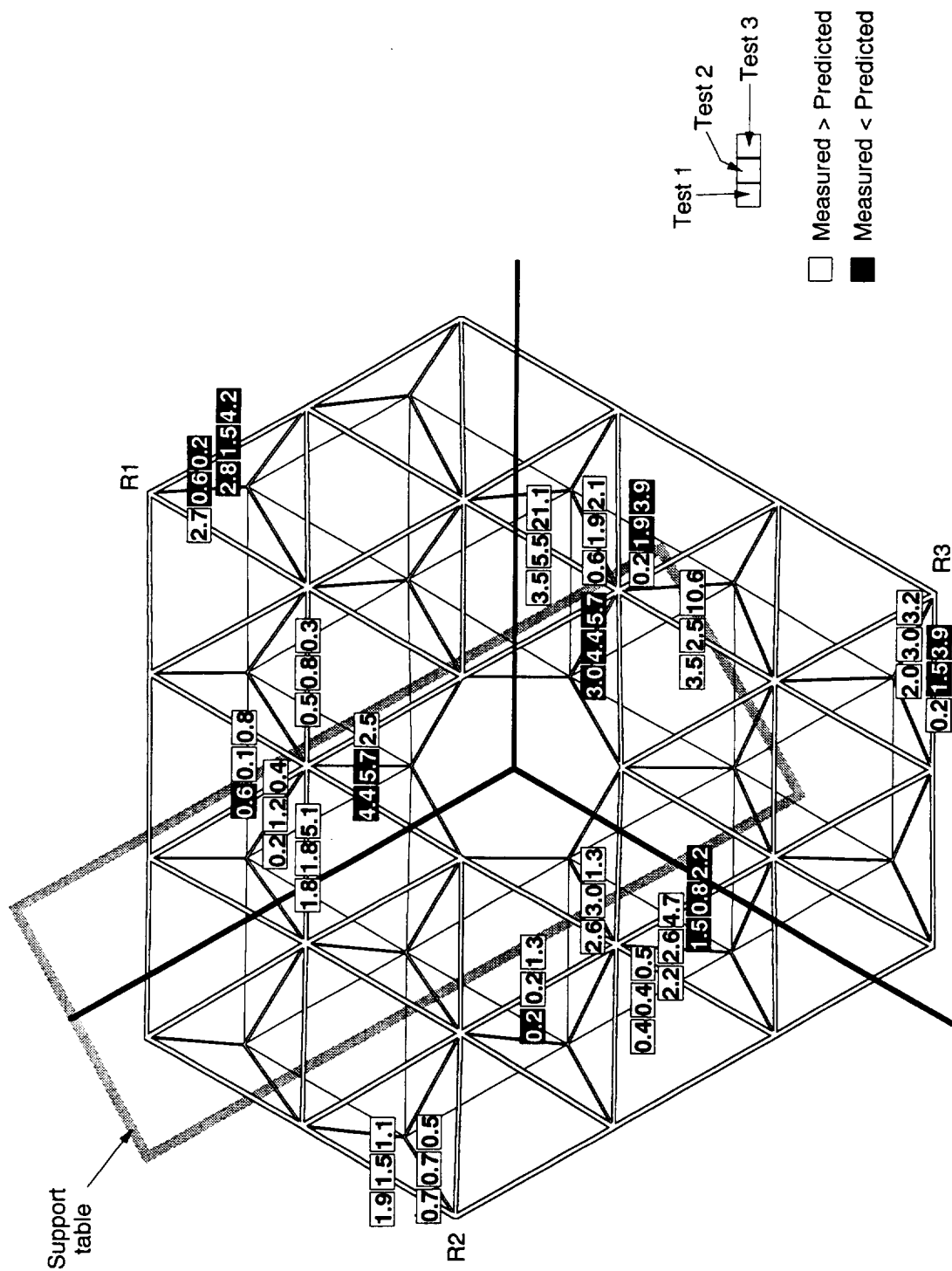


Figure 15. Differences between measured and predicted strain magnitudes for static tests 1, 2, and 3. Differences are in inches per inch and should be multiplied by 10^{-6} .

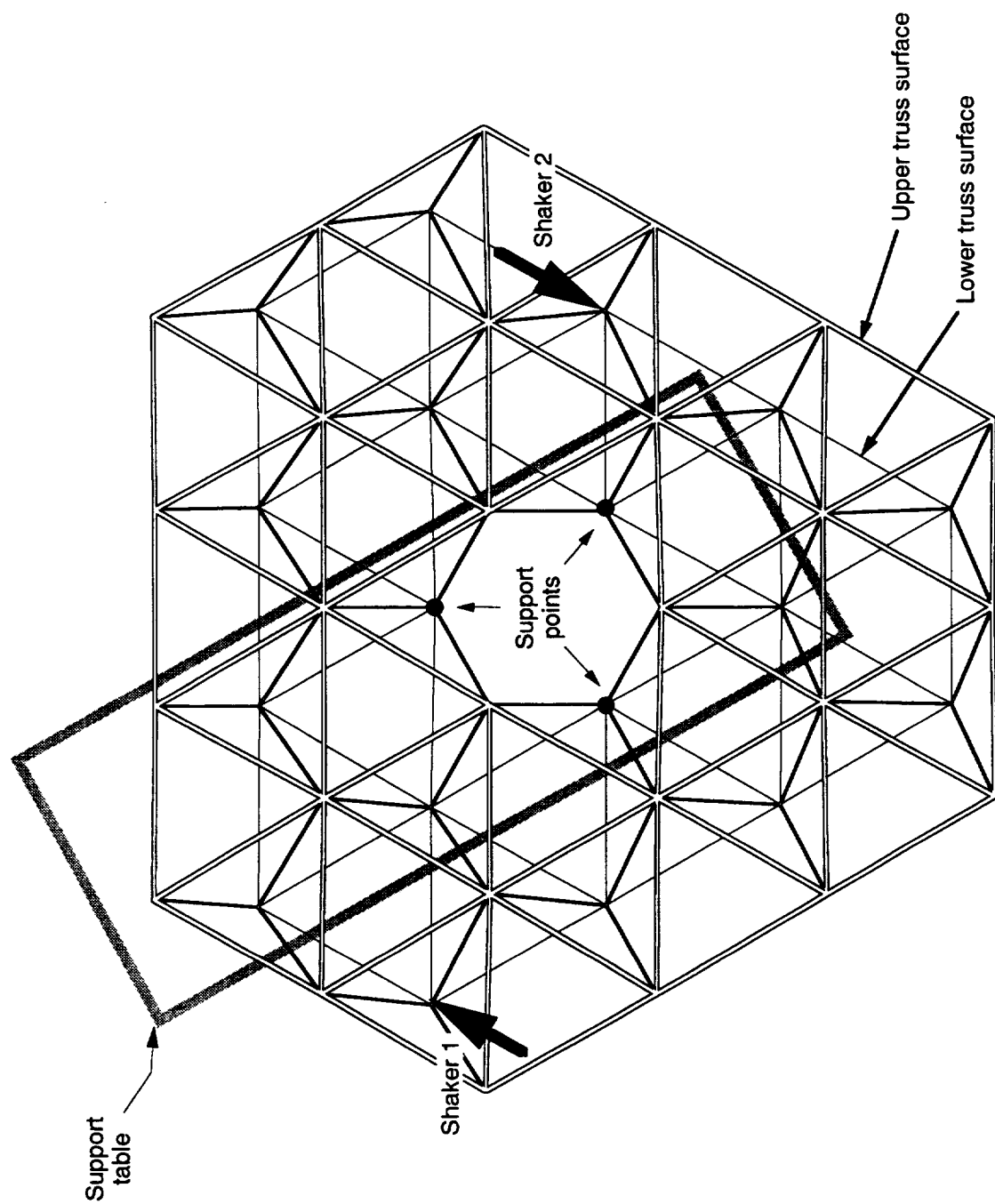
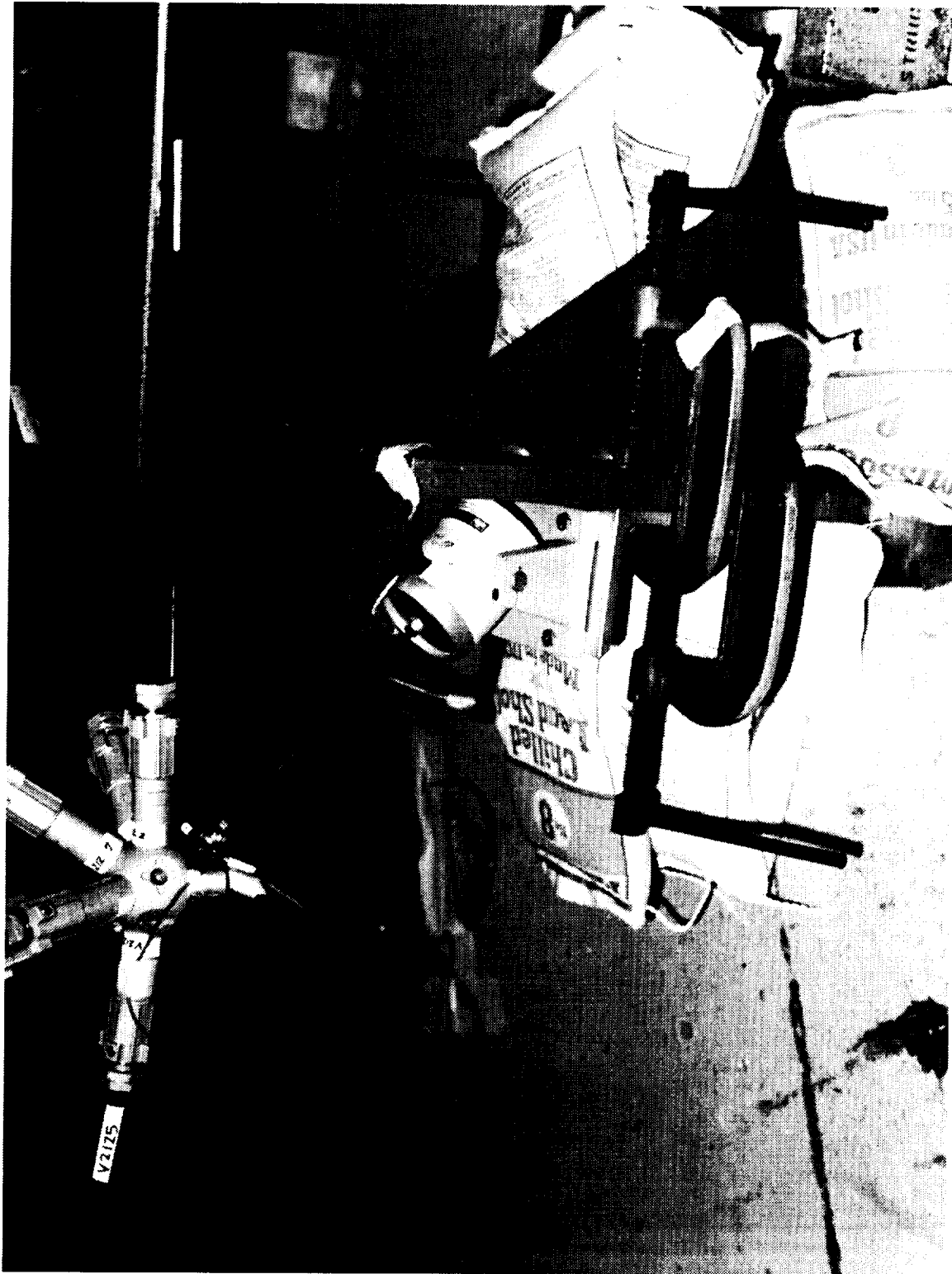
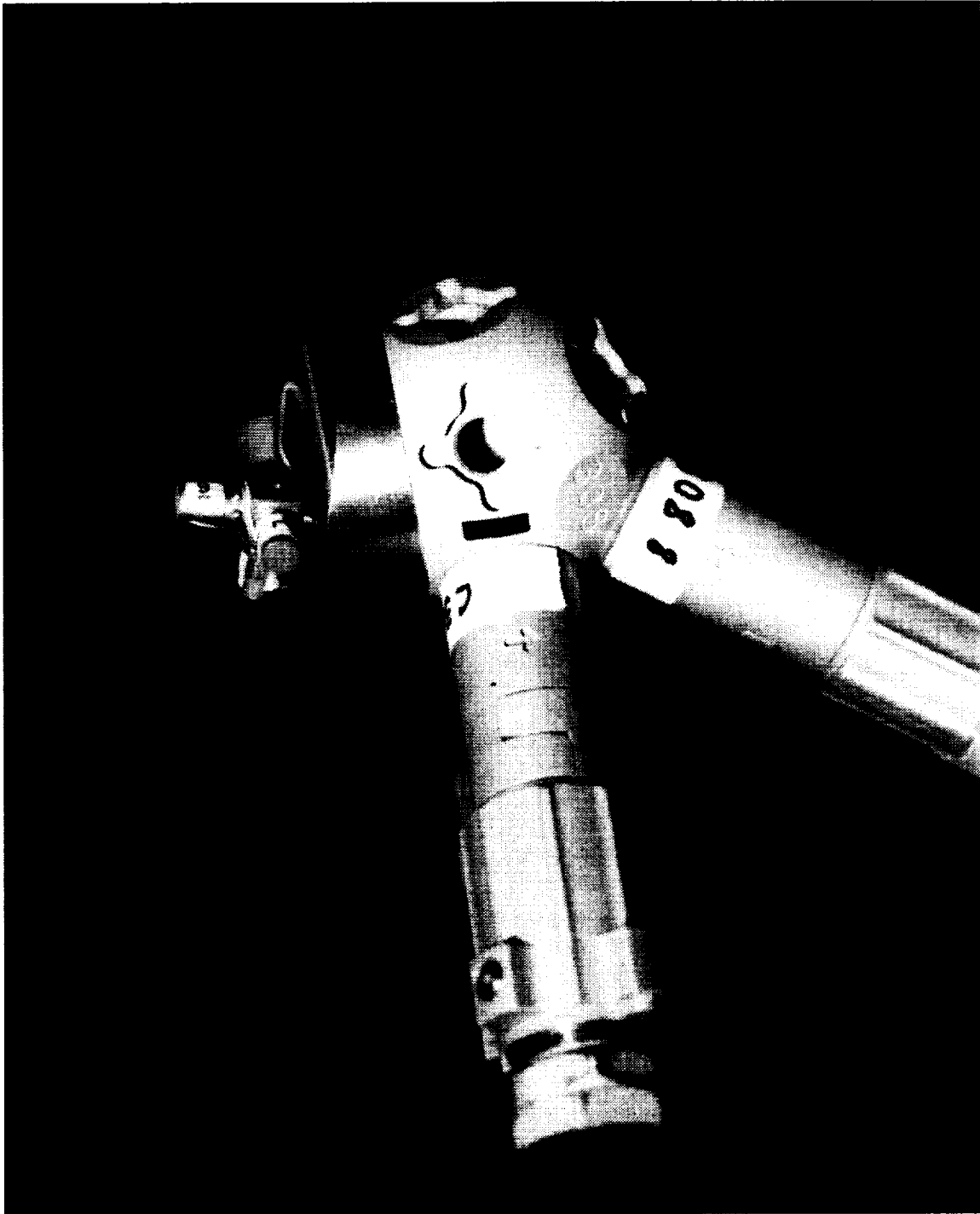


Figure 16. Shaker locations and input force directions (planform view) for dynamic testing.



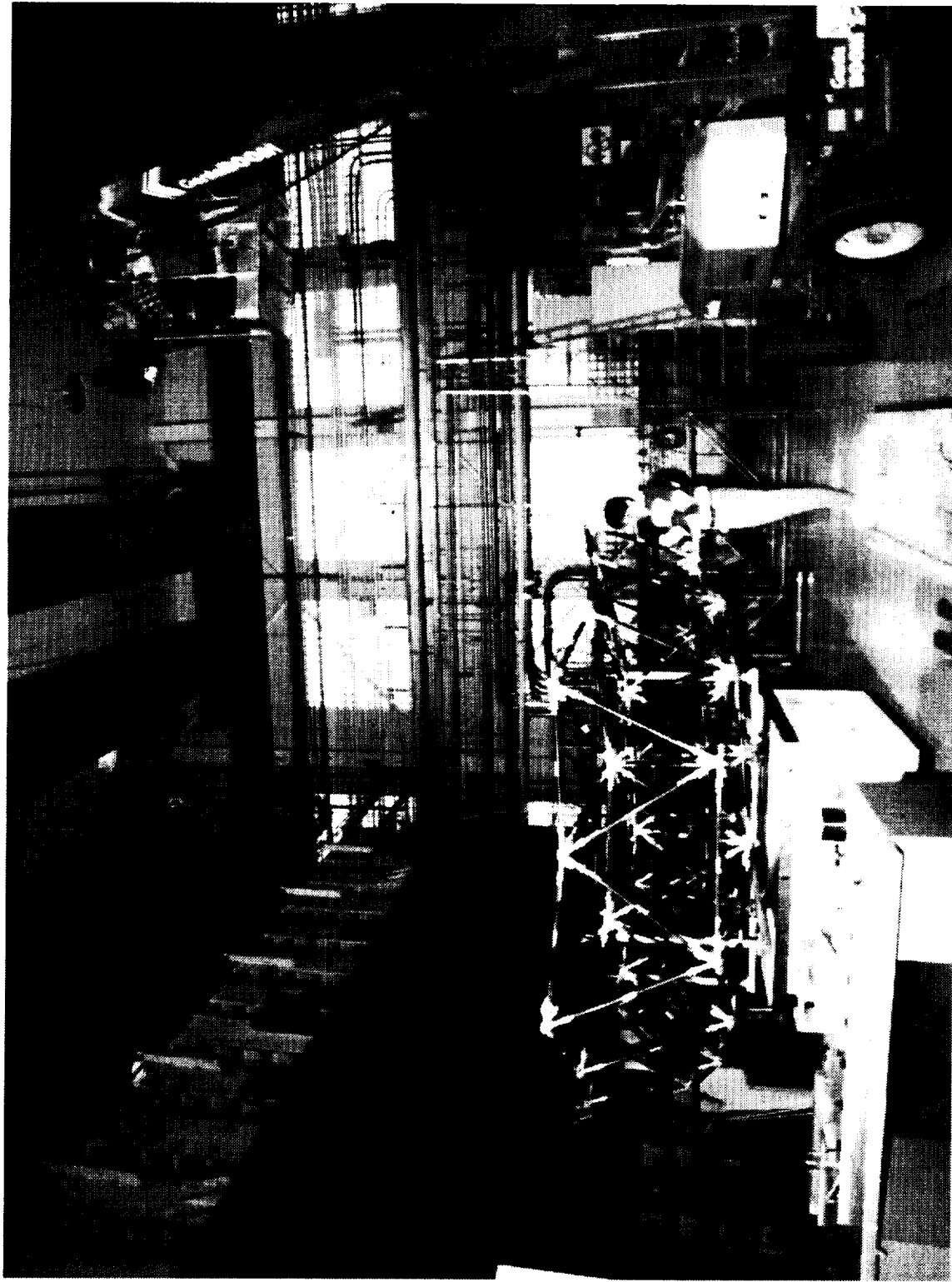
L-89-14197

Figure 17. One of two shakers used to excite structural modes.



L-89-14198

Figure 18. One of 45 triaxial accelerometers used to measure dynamic response.



L-90-04508

Figure 19. Truss and elevated photogrammetric camera.

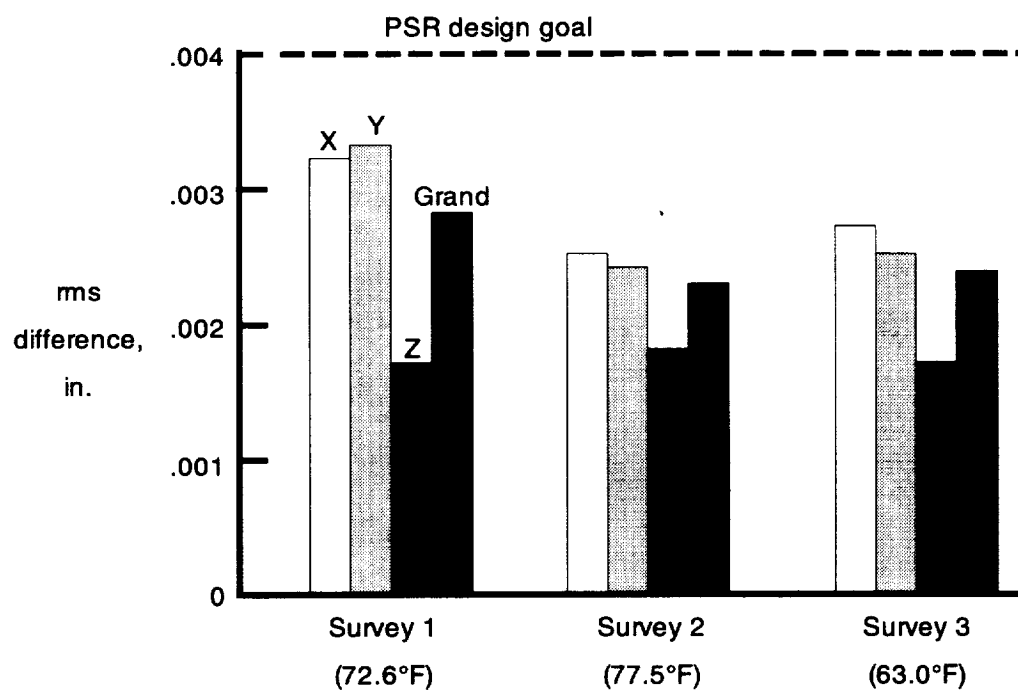


Figure 20. Root-mean-square differences between photogrammetrically measured and predicted target coordinates.

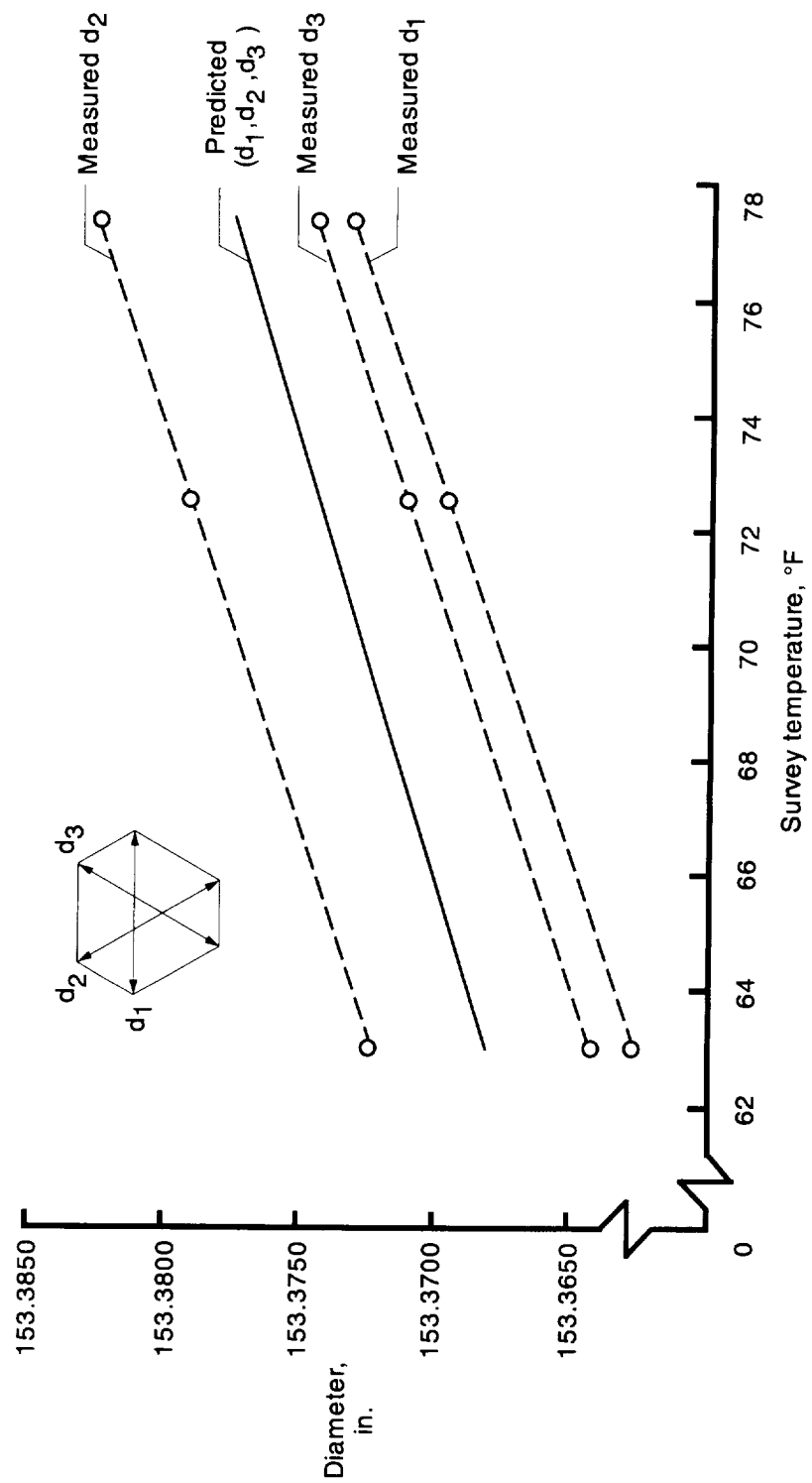


Figure 21. Measured and predicted truss diameters as a function of survey temperature.

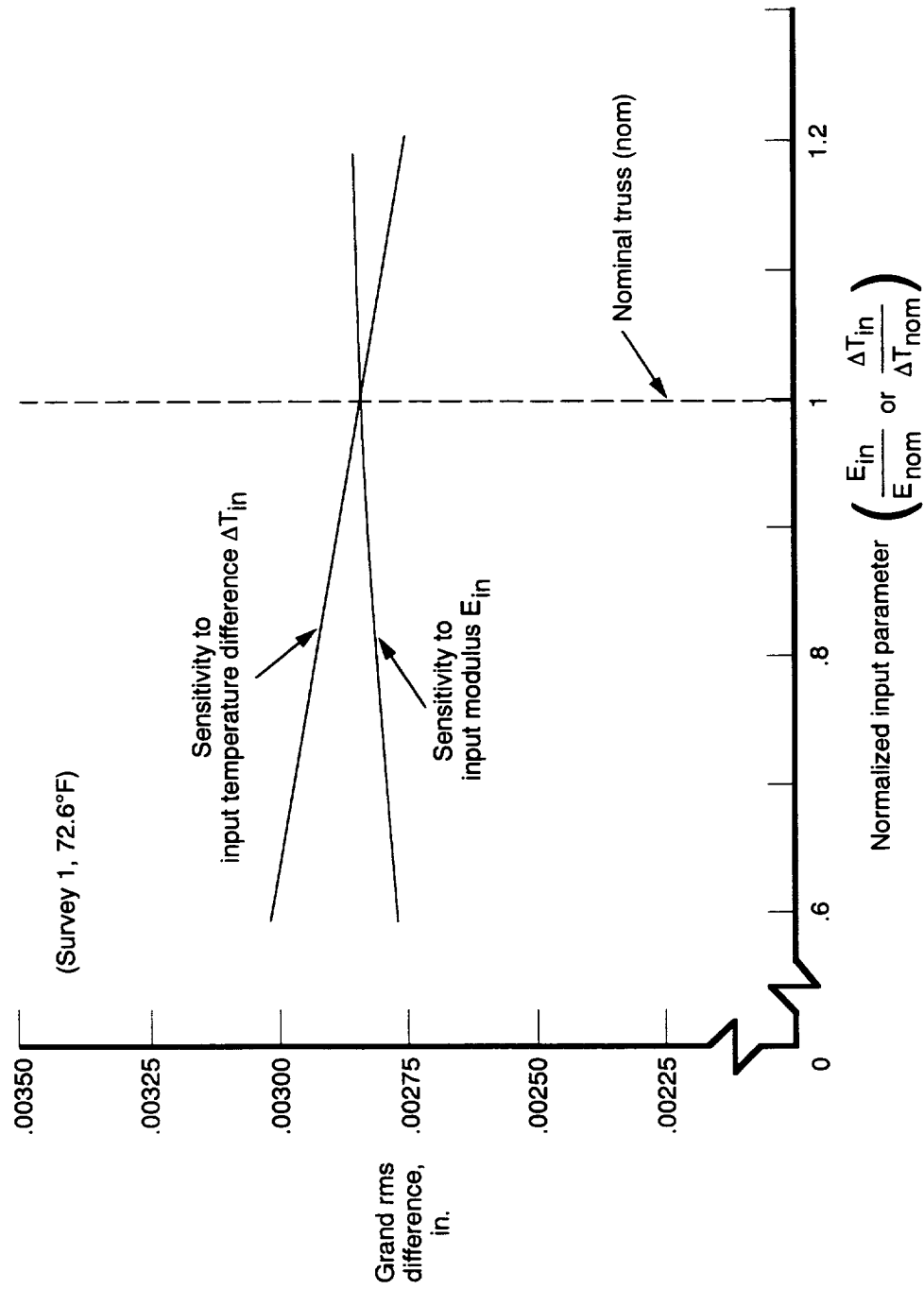


Figure 22. Sensitivity of rms difference to finite-element-model input values for strut modulus and strut temperature change.

REPORT DOCUMENTATION PAGE			Form Approved OMB No. 0704-0188	
Public reporting burden for this collection of information is estimated to average 1 hour per response, including the time for reviewing instructions, searching existing data sources, gathering and maintaining the data needed, and completing and reviewing the collection of information. Send comments regarding this burden estimate or any other aspect of this collection of information, including suggestions for reducing this burden, to Washington Headquarters Services, Directorate for Information Operations and Reports, 1215 Jefferson Davis Highway, Suite 1204, Arlington, VA 22202-4302, and to the Office of Management and Budget, Paperwork Reduction Project (0704-0188), Washington, DC 20503.				
1. AGENCY USE ONLY (Leave blank)	2. REPORT DATE July 1995	3. REPORT TYPE AND DATES COVERED Technical Paper		
4. TITLE AND SUBTITLE Structural Analysis and Testing of an Erectable Truss for Precision Segmented Reflector Application		5. FUNDING NUMBERS WU 233-01-01-01		
6. AUTHOR(S) Timothy J. Collins, W. B. Fichter, Richard R. Adams, and Mehzad Javeed				
7. PERFORMING ORGANIZATION NAME(S) AND ADDRESS(ES) NASA Langley Research Center Hampton, VA 23681-0001		8. PERFORMING ORGANIZATION REPORT NUMBER L-17426		
9. SPONSORING/MONITORING AGENCY NAME(S) AND ADDRESS(ES) National Aeronautics and Space Administration Washington, DC 20546-0001		10. SPONSORING/MONITORING AGENCY REPORT NUMBER NASA TP-3518		
11. SUPPLEMENTARY NOTES Collins, Fichter, and Adams: Langley Research Center, Hampton, VA; Javeed: Lockheed Engineering & Sciences Company, Hampton, VA.				
12a. DISTRIBUTION/AVAILABILITY STATEMENT Unclassified-Unlimited Subject Category 18 Availability: NASA CASI (301) 621-0390		12b. DISTRIBUTION CODE		
13. ABSTRACT (Maximum 200 words) This paper describes analysis and test results obtained at Langley Research Center (LaRC) on a doubly curved test-bed support truss for precision reflector applications. Descriptions of test procedures and experimental results that expand upon previous investigations are presented. A brief description of the truss is given, and finite-element-analysis models are described. Static-load and vibration test procedures are discussed, and experimental results are shown to be repeatable and in generally good agreement with linear finite-element predictions. Truss structural performance (as determined by static deflection and vibration testing) is shown to be predictable and very close to linear. Vibration test results presented herein confirm that an anomalous mode observed during initial testing was due to the flexibility of the truss support system. Photogrammetric surveys with two 131-in. reference scales show that the root-mean-square (rms) truss-surface accuracy is about 0.0025 in. Photogrammetric measurements also indicate that the truss coefficient of thermal expansion (CTE) is in good agreement with that predicted by analysis. A detailed description of the photogrammetric procedures is included as an appendix.				
14. SUBJECT TERMS Space antennas; Erectable structures; Lightweight trusses; Finite elements			15. NUMBER OF PAGES 39	
			16. PRICE CODE A03	
17. SECURITY CLASSIFICATION OF REPORT Unclassified	18. SECURITY CLASSIFICATION OF THIS PAGE Unclassified	19. SECURITY CLASSIFICATION OF ABSTRACT Unclassified	20. LIMITATION OF ABSTRACT	

